Enhanced Structural, Dielectric, and Magnetic Properties of Mn-Yb-doped Y-type Hexaferrites

Muhammad Nadeem (nadeemmalik12307@gmail.com)
Islamia University of Bahawalpur: The Islamia University of Bahawalpur Pakistan
https://orcid.org/0000-0001-8600-5563

Hasan Mehmood Khan
Islamia University of Bahawalpur: The Islamia University of Bahawalpur Pakistan
https://orcid.org/0000-0002-9440-5580

saeed ahmad Buzdar
Islamia University of Bahawalpur: The Islamia University of Bahawalpur Pakistan

Javed Ahmad
BZU: Bahauddin Zakariya University

Muammad A Asari
King Khalid University College of Medicine

Muhammad mran
King Khalid University College of Medicine

Ambreen Aleem
Islamia University of Bahawalpur: The Islamia University of Bahawalpur Pakistan

mehrun nisa
The Government Sadiq College Women University Bahawalpur

Muhammad Ehsan Raza
BZU: Bahauddin Zakariya University

Research Article

Keywords:

Posted Date: September 14th, 2022

DOI: https://doi.org/10.21203/rs.3.rs-2022724/v1

Abstract

This study aimed to determine the effect of Mn^{2+} and Yb^{3+} ions substitution on the structural, dielectric, morphological, and magnetic properties of $CaBaCo_{2-x}Mn_xYb_yFe_{12-y}O_{22}$ where x = 0.00-0.1 and y = 0.00-0.01 Y-type hexagonal ferrites prepared by sol-gel auto combustion. For 6 hours, samples were calcined at 1050 degrees Celsius. X-ray diffraction (XRD) analysis was used to study the formation phase of Y-type hexaferrites. The calculated structural auxiliary parameters, such as lattice constants (a and c), cell volume (Vcell), X-ray density (dx), bulk density (db), and porosity (P), were found to be within the following ranges: a = 5.891 to 5.9Å, c = .43.466 to 43.543Å, Vcell 1310.53 to 1312.26$Å^3$, dx = 5.01 to 5.05(g/cm^{-1}) db = 2.622 to 3.032 (g/cm^{-1})and P = 39.969 to 47.665%. The location of the ions, including their respective bonds, inside the structure of the lattice matrix, was revealed by Fourier-transform infrared spectroscopy (FTIR). SEM pictures confirmed the plate-like shape of the particles, confirming the XRD findings. In the dielectric analysis, the typical dielectric response of ferrites was observed. Grain contribution is low when compared to grain boundaries contribution The generated Y-type hexaferrites samples' multidomain magnetic nature resulted in domain wall displacement, which affects the coercivity values. A vibrating sample magnetometer was used to investigate magnetic characteristics (VSM). The saturation magnetization (Ms), Retentivity (Mr), and coercivity (Hc) of the material were found to be 4.11 to 2.21 emu/g, 2.33 to 1.22emu/g, and 1776.78 to 2283,51Oe, respectively. These powders can be used as pre-eminent contender materials for perpendicular recording media (PMR) applications.

Corresponding Author’s E-mail: hmkhan@iub.edu.pk

1 Introduction

Ferrites, such as spinel, garnet, and hexagonal ferrite, have captivated scientists' interest because of their tunable magnetic, dielectric, and optical properties, as well as potential applicability in domains including electromagnetic wave absorption and magnetic memory. Hexagonal ferrite has exhibited some of the most intriguing features since its discovery by Philips in the 1950s, as they can be hard or soft

magnetic materials based on their chemical compositions [1–6]. Due to their low cost, ease of fabrication, and remarkable electrical and magnetic properties, hexaferrites are among the most important materials today. Y-type hexaferrites with planar magnetic anisotropy have a larger magnetic permeability in the GHz frequency range than other hexagonal ferrites having uniaxial magnetic anisotropy, which is interesting to many researchers [7–9]. Hexaferrites are classified into different types based on their chemical composition, such as M-, Y-, Z-, X-, U-, and W-type hexagonal ferrites [10–13]. The Y-type hexagonal ferrites' crystalline structure was described as an alternating stacking of the S and T blocks along the c-axis with space group R-3m [14–16]. Furthermore, the Y-type hexagonal ferrite belongs to the R-3m space group, with a magnetic structure consisting of the S- and T-spin blocks along the c-axis, with the S-block containing AFe4O8, and the T-block including A2Fe8O14, where A is a divalent metal ion. 3aVI, 3bVI, 18hVI, 6cVI, 6cIV, and 6c*IV are the crystallographic positions occupied by Fe^{3+} in the S- and T-blocks. Three of the sites were spin-ups (3aVI, 3bVI, and 18hVI), whereas the other three (6cIV, 6cVI, and 6c*IV) were spin-

downs [17]. Two separate magnetic blocks can be characterized based on the relative direction of magnetic moments in each layer: The magnetic moments of the Fe ions were organized in a collinear way within each block, with small (S) and large (L) magnetic moments [18]. Many researchers changed the orientations of the spins on the sites of Y-type hexaferrites to improve their magnetic characteristics by substituting the Me2 + and Fe^{3+} ions with transition metals, rare-earth metals, or a combination of both. Lee and Kwon, for example, looked at the magnetic characteristics of a $Co_{2-x}Zn_xY$-type barium hexaferrites [19]. The solid-state reaction approach, the microemulsion method, the co-precipitation method, and the sol-gel method have all been utilized to synthesize Y-type hexaferrites. The sol-gel method, on the other hand, has several advantages, including good microstructure control, high chemical homogeneity, and a quick reaction time, as well as the method's simplicity, the highest crystallinity and purity of the samples, narrow size distribution, and high surface area of the particles, as well as low cost [17, 20].

Motivated by the review of literature, we proceeded to synthesize and characterize Yb^{3+}–Mn^{2+}-substituted Y-type calcium barium hexaferrites. Substituting rare earth (RE) elements (such as Yb^{3+}) in the hexagonal lattice structure could lead to the modification of the magnetic properties of the prepared samples. This is because RE elements possess large magneto crystalline anisotropy as a result of the presence of localized electrons [6]. The electrical and magnetic characteristics of materials can be affected as their size is lowered to the nanoscale. Because of their small size, nanostructures can be formed to obtain certain qualities [21]. The magnetic and dielectric properties are affected by a variety of elements, including synthetic procedure, sintering temperature, cation substitution, and composition. The current research study's major goal is to look at the relationship between numerous structural factors and the level of substitution by divalent and trivalent metal ions. Even though the dielectric properties and magnetic behavior of hexaferrites in the nano regime have been researched and have led to various applications, our understanding of the dielectric characteristics of Yb–Mn substituted Y-type hexaferrites in the nano regime is currently insufficient. The use of transition metal and rare earth cations as dopants considerably improves the structure, magnetic properties, and dielectric response of hexaferrites. This is an intriguing and difficult aspect that has to be researched in order to fully comprehend the dielectric and magnetic properties of these hexaferrites. The frequency-dependent quality factor and ac conductivity are intriguing parameters that suggest that these hexaferrites could be used in a variety of technological applications. Investigation of magnetic characteristics gives information regarding exchange interactions and is anticipated to improve our understanding of how cations occupy lattice positions [22]. The purpose of this research is to investigate the effects of Yb^{3+} and Mn^{2+} ion substitutions on the structural, magnetic, and dielectric properties of Co_2Y-type barium hexaferrites. X-ray diffraction (XRD), Fourier-transform infrared (FTIR) spectroscopy, scanning electron microscopy (SEM), impedance analysis, as well as vibrating-sample magnetometer (VSM) measurements were used to characterize the prepared samples

2 Experimental

Calcium nitrate $Ca(NO_3)_2$ 99.9%, Barium nitrate $Ba(NO_3)_2$ 99.9%, Cobalt nitrate $Co(NO_3)_2$ 99.9%, Manganese nitrate $Mn(NO_3)_2$ 99.9%, Ytterbium nitrate N_3O_9Yb 99.9% ferric nitrate $Fe(NO_3)_2.9H_2O$ 99.9%, Without additional purification, all chemicals and reagents were utilized as obtained. We dissolved stoichiometric proportions of the chemicals in 100 mL of distilled water in the appropriate measurement to synthesize nanoparticles of the $CaBaCo_{2-x}Mn_xYb_yFe_{12-y}O_{22}$ where x = 0.00-0.1 and y = 0.00-0.01 Y-type hexaferrites Then, with a 1:1 molar ratio of cations to citric acid, we added citric acid. To get the pH of the solution to 7.0, we used a drop-by-drop addition of ammonia solution. At roughly 85^0C the solution was agitated using a magnetic stirrer resulting in the creation of a gel-like solution after about 6 hours. We placed the gel-like solution on a hot plate as well as heated it to roughly 350 degrees Celsius; this allowed the gel-like solution to self-combust forming the precursor substance. Finally, to obtain the required Y-type phase we sintered the precursor material at 1050ºC for 6 hours.

The phase of the generated samples was determined using a powder X-ray diffractometer (Bruker D8 Advance) with Cu-Ka as the radiation source and diffraction angles ranging from 10 to 90 in increments of 0.02, followed by FTIR with diamond ATR. The related functional groups were found using FTIR spectra collected with the Nicolet FTIR interferometer IR prestige-21 in the 400–4000 cm-1 area (model8400S). The morphology of the manufactured samples was examined using FESEM (MIRA3 TESCAN, USA). An Agilent RF Impedance analyzer was used to perform the dielectric test at room temperature (27oC) (model: E4991a). The M-H hysteresis loop was acquired using a vibrating sample magnetometer (Lakeshore 7410) to examine the magnetic characteristics of the manufactured samples.

3 Results And Discussion

3.1 XRD analysis

The corresponding XRD patterns of calcined materials with varying Mn-Yb concentrations are shown in Fig. 1. The samples' observed peaks were compared to those on the standard JCPDS card # 44–0206. The usual Y-type hexagonal ferrites are represented by all peaks. according to a close examination of the patterns/ Moreover, at higher Mn-Yb concentrations Sharp, well-defined, and powerful diffraction peaks are present in all patterns, indicating the production of a well-crystallized Mn-Yb replacement CaBaCo based Y-type hexaferrites structure.

The following equations were used to derive structural characteristics like crystallite size, lattice constants (a and c), as well as the c/a ratio [23, 24] unit cell volume, and X-ray density [25, 26], and porosity.

$$D = K\lambda/\beta\cos\theta_\beta \quad (1)$$

$$1/d^2 = 4/3((h^2 + hk + K^2)/d^2) + l^2/c^2 \quad (2)$$

$$V = a^2c\sin120^o \quad (3)$$

$$d_b = m/\pi r^2 h \quad (4)$$

$d_x=ZM/N_AV_{cell}$ (5)

$P = 1-d_b/d_x$ (6)

where is the wavelength of the radiation used, is the pattern's strongest peak's whole width at half maximum, is the diffraction angle, d is the distance between lattice planes, hkl are miller indices, and a and c are lattice parameters respectively. Each synthesized sample's crystallite size was estimated using the well-known Scherer formula (Eq. 1). The crystallite diameters are all between 27.3 and 37.1 nm. In Fig. 2, a plot depicting the fluctuation of lattice constants a and c with Mn-Yb content is displayed. The difference in ionic radii can explain the increase in lattice constants increasing Mn-Yb content. The ionic radius of the Mn^{2+} (0.83 Å) ion is greater than that of the Co^{2+} (0.78 Å) ion. The c/a ratio, on the other hand, ranges from 7.367 to 7.381, indicating that it is within the range of Y-type hexagonal ferrites [23, 27]. Because the Y-type hexagonal structure is made up of three overlapping T and S blocks and oxygen layers [3(TS)] [27], With a value of 3, Z stands for the effective number of molecules per unit cell.

The sample's molecular mass is M, its Avogadro number is N_A, and its unit cell volume is Vcell. From Equations (3) and (4) bulk density db and X-ray density dx were calculated respectively and their variation is shown in Fig. 3. The projected values of these parameters for our specimens are shown in Table 1.

Table 1
The calculated values of lattice parameters, cell volume, crystalline size, x-ray density, bulk density, porosity for CaBaCo2-xMnxYbyFe12-yO22 where x = 0.00 to 1.0 and y = 0.00 to 0.1 hexagonal ferrites.

Compositions	a(Å)	c(Å)	c/a	V_{cell} $(Å)^3$	Crystalline size (nm)	d_x (g/cm^{-1})	d_b (g/cm^{-1})	Porosity (%)
x = 0.00, y = 0.00	5.9	43.466	7.367	1310.53	27.3	5.01	2.622	47.66588
x = 0.20, y = 0.02	5.891	43.506	7.385	1307.34	30.6	5.03	2.722	45.8794
x = 0.40, y = 0.04	5.893	43.483	7.378	1307.99	32.5	5.04	2.654	47.34548
x = 0.60, y = 0.06	5.894	43.502	7.380	1308.83	29.8	5.04	2.999	40.4955
x = 0.80, y = 0.08	5.896	43.522	7.381	1310.21	34.8	5.05	2.935	41.88073
x = 1.00, y = 0.10	5.899	43.543	7.381	1312.26	37.1	5.05	3.032	39.96968

Moreover, unit cell volume increased uniformly with Mn-Yb concentration, which was attributable to an increase in lattice characteristics. Theoretical X-ray density decreased slightly, which is due to Mn-Yb lower atomic mass compared to Co and the inverse relationship between unit cell volume and X-ray density as seen in Eq. (5). The percentage porosity, on the other hand, also drop from 47.665 to 39.969 possibly due

to an enhancement in X-ray density and a difference in the atomic radii of the dopant and host ions Fig. 4 describes the trend of porosity (P) and bulk density (db) with increasing the concentration of dopants [23, 28]. Variation in crystalline size with mn-Yb dopant can be seen in Fig. 5.

3.2 SEM analysis

The microstructures of $CaBa_2Co_{2-x}Mn_xYb_yFe_{12-y}O_{22}$ specimens sintered at 1050^oC for 6 h with varying amounts of Mn-Yb concentration are shown in Fig. 6. Prepared nanoparticle particles are uniformly dispersed, with well-defined spherical and platelet-like forms, as shown by SEM micrographs. Hexaferrites with a platelet form are best for microwave absorption [29]. A close examination of the photos demonstrates that grain size increases as Mn content rises. Figure 4.38 illustrates that at greater Mn concentrations, agglomerated nanoparticles are found. This agglomeration can be explained by the strong magnetic dipole, Van der Waals contacts among some of the particles, or the chemical reaction that happens between the particles during the calcination process [23]. The SEM pictures show that the samples were manufactured in the nano-regime (grain sizes vary from 68 to 77 nm). The grain size was determined using a formula previously published [30 ur Raheem, 2017 #270]. The images revealed that the parts are crack-free as well as tightly packed together. The hexagonal structure of the synthesized substances was confirmed by the platelet-like structure seen in Fig. 6.

3.3 FTIR analysis

The chemical bonding, as well as structural changes in CaBaCo2-xMnxYbyFe12-yO22 (where x = 0.00 to 1.0 and y = 0.00 to 0.1) nanoparticles generated by the sol-gel technique, was investigated using Fourier transform infrared spectroscopy (FTIR). FTIR spectra of Mn-Yb substituted $CaBaCo_2$-Y type hexagonal ferrites with Mn-Yb varying concentrations from x = 0.00 to 1.0 and y = 0.00 to 0.1 are shown in Fig. 7. The metal-oxygen stretching vibrations of hexaferrites were identified in the absorption spectra of calcined samples as two distinct peaks in the low-frequency band [31]. The greatest peaks in the range of 554-592cm^{-1} were attributed to the intrinsic vibration of octahedral sites, while the lowest peak at 433cm^{-1} revealed the typical interaction among oxygen as well as metal cations of tetrahedral sites [32–34]. Because of the variation in the number of divalent cations in tetrahedral and octahedral sites, it was expected to observe differences in the intensity of the bands in varied compositions. All ferrites have these two bands as their distinguishing features. These bands are indicative of the development of metal ions-oxygen bands in the hexagonal, as previously described.

The variation in the wavelength of bands for the prepared sample could be due to differences in cation mass, cation-oxygen separation, and bonding forces [35, 36]. The asymmetric stretching vibrations of metal cations at tetrahedral and octahedral sites lattice sites are seen in this Fig. 7 as absorption bands in the range 400cm^{-1} to 600cm^{-1}, which also correspond to the asymmetric stretching vibrations of metal cations at tetrahedral and octahedral lattice sites [37]. A popular illustration of spinel ferrite structure is a low-frequency band about 400cm^{-1} and a high-frequency band around 500-600cm^{-1}. These bands are ascribed to cations vibrations in the spinel block of Y-ferrite in a hexagonal structure. It has been observed

that as Mn concentration is increased, v1 moves toward higher wavenumber values, while v2 shifts toward lower wavenumber values. This steady shift in both bands can be linked to the substitution of cations with higher ionic radius, which impacts cation-anion stretching between octahedral and tetrahedral lattice sites as a result. The metal-oxygen-metal bands such Co-O-Co and Fe-O-Fe, which emerge about 1100-500cm^{-1}, correspond to the absorption peaks [38]. The H-O-H bending vibrations of absorbed water molecules are represented by the peaks at 1620, 2025, and 2350cm^{-1} [23, 39, 40].

3,4 Dielectric properties

3.4.1 Dielectric constant (ε_0)

The dielectric constant (ε_0) is essential to find out how far an electromagnetic signal can pass through a substance. By a factor equal to the square root of the dielectric constant microwaves reaching dielectric materials gain a low speed. "The electrically charged energy stored per unit volume and unit potential gradient" is another way of putting it. When applied as a capacitor, it represents the material's ability to hold the charge [41–43]. Mathematically, it's as follows:

$\varepsilon = Cd/A\varepsilon_0$ (7)

"C" stands for capacitance in farads, "d" for pellet width in meters, and "A" is for the area of cross-section of the specimen [44, 45]. Figure 8 shows the fluctuation of the dielectric constant concerning the frequency of the applied field for all $CaBaCo_{2-x}Mn_xYb_yFe_{12-y}O_{22}$ (where x = 0.00 to 1.0 and y = 0.00 to 0.1) nano-ferrite composition. At high frequencies, the fluctuation throughout the dielectric constant (ε_0) was relatively moderate compared to low frequencies, confirming the distinct fluctuations of the dielectric constant (') at different frequencies. High resistive grain boundaries lead to high values of E at lower frequencies, while low resistive grain boundaries cause low values of E at higher frequencies. The frequency in-dependent response was seen at higher frequencies over 3 GHz. The space charges polarizing and hooping conduction among Fe^{3+} and Fe^{2+} ions could explain the broad changes at high frequencies. The well-known Maxwell- Wagner model and Koop's hypothesis are in agreement with this interpretation [46].

The dielectric dispersion is attributable to dipole relaxation under lower frequency values, while at higher frequencies, these resonance peaks are dependent on the applied frequency whereas charging transfer frequency between Fe^{2+} and Fe^{3+} ions, i.e. ionic relaxation. The heterogeneous dielectric properties of a substance are fundamental for space charge polarisation, according to the Maxwell and Wagner model and Koop's hypothesis. Ferrites have inter-grain boundaries among high conductivity phases (grains) as well as low conductivity matrices (grain borders). One of the most common causes for the decrease in along with the greater frequency of the applied field would be that the grain boundaries become highly resistive at a certain point, causing electrons to hop heaps up there and produce polarisation. When the applied frequency increases further, the electrons reverse their travel destructively, reducing their chances of finding the grain boundary, and, as a result, the polarization decreases [47]. Due to a substantial

amount of Fe^{2+} ions at octahedral sites, the electronic transfer between Fe^{2+} and Fe^{3+} has been observed to be greater. When the applied alternating field frequency exceeds 2 GHz, the jumping frequency of electrons between Fe^{2+} and Fe^{3+} ions equals the applied alternating field frequency [44, 48]. When ions oscillate uniformly on both sides, the applied ac field frequency and natural frequency become equal, and power loss increases, which is why resonance peaks appear [49].

3.4.2 Dielectric loss factor (ε_0)

The fluctuations in the imaginary dielectric constant (") as a function of frequency are shown in Fig. 9. At the applied frequency, all of the samples revealed a decreasing trend in the imaginary dielectric constant. The dielectric constant (') seems qualitatively equivalent to the reduction in the imaginary dielectric constant ("). The magnitude of the imaginary dielectric constant (") decreases as the applied frequency rises, eventually reaching a minimum value and becoming constant. A considerable number of conducting grains are found in ferrites that are separated via insulating grain borders.

It has already been shown that grain boundaries are effective at lower frequencies, although conductive grains become efficient at higher frequencies. As a result, ferrite materials have low polarisation when compared to other materials at higher frequencies. The resonance peak seen at lower frequencies is due to space or interfacial polarization, whereas the resonance peak seen at higher frequencies could be due to constructive interferences between the natural frequency of the ions and the frequency of the applied electric field. Ion frequency and applied electric field frequency Extended ionic relaxation may be affected by different metal ions having numerous valance states. In the current investigation, Fe was replaced with Yb, which resulted in a decrease in the relaxation peak intensity. The number of various valence state cations affects the relaxation peak intensity. The number of Fe entities in ferrites reduces whenever Yb is substituted, followed by a drop in the number of distinct valence state cations, i.e. Fe^{2+}/Fe^{3+}. As a result of this substitution, electron hopping among Fe^{3+} and Fe^{2+} diminishes, resulting in a reduction in relaxation peak intensity.

3.4.3 Tan loss (tanδ)

The energy dissipation in a dielectric medium is calculated using the loss tangent (tanδ). It could be used to determine how much electromagnetic energy is dissipated naturally. It is determined by the equation and represents the tangent of the angle in a complex plane between both the resistive and reactive components.

$$Tan\delta = \varepsilon'/\varepsilon \quad (8)$$

Tangent loss is explained by the following mathematical formula of ac conductivity.

$$Tan\delta = \sigma_{ac}/2\pi f\varepsilon \quad (9)$$

The tan loss (Tanδ) is proportional to σac as well as inversely proportional to the dielectric constant ('). Figure 10 shows the pattern of tangent loss (Tanδ) fluctuation over frequency for $CaBaCo_{2-}$

$_xMn_xYb_yFe_{12-y}O_{22}$ nano-ferrites at normal temperature. Certain resonance peaks have been discovered above 2 GHz, among both x = 0.6, y = 0.06, and. From x = 0.8, y = 0.08 It is almost constant at lower frequencies, however. The main causes of tanδ dispersion are similar to those of dielectric constant (') dispersion. Rezlescu model explained that, in ferrites, the dielectric polarisation mechanism is analogous to the conduction mechanism [50] When the relaxation period and applied field frequency are equal in a dielectric substance, the phase lag of the dipole oscillation develops, which can be characterized using dielectric tanδ. The Tanδ is determined by nature. When the relaxation period and applied field frequency are equal in a dielectric substance, the phase lag of the dipole oscillation develops, which can be characterized using dielectric Tanδ. The Tanδ is determined by the type and quantity of ions present [51, 52]. The primary factors that affect dielectric characteristics of nano-ferrites include processing techniques, particle size, sintering temperature, cation distribution, Fe^{3+}/Fe^{2+} ions ratio, stoichiometry, compositional homogeneity, oxygen vacancies, and a few other parameters [53]. Because the displacement of Fe^{3+} ions, as well as oxygen vacancies, leads to increasing Mn-Yb doping, all-dielectric properties have greater values than the pure sample.

Undoped samples have fewer oxygen vacancies, which increases conductivity and results in low electrical characteristics. Because the ionic radius of Yb^{3+} is higher than that of Fe^{3+}, the unit cell volume rose. The available free volume for Fe^{3+} ion mobility increases, resulting in higher electrical characteristics [54, 55].

3.4.4 AC conductivity (σac)

The ability of a material to conduct electric current is known as specific conductance or electrical conductivity (σ_{ac}). It can be stated mathematically as the sum of two terms, as shown below.

$\sigma_{ac} = \sigma_1 (T) + \sigma_2 (\omega,T)$ (10)

The first term in this formula, "σ_1 (T)" is dc electrical conductivity, which is frequency independent. It is contingent on the free charge carriers' drift mobility. The second term, σ_2 (ω, T) is related to dielectric relaxation and thus is frequency as well as temperature-dependent [56]. σ_2 (ω, T) is governed by a power law.

$\sigma_2 (\omega, T) = B(T)\omega^{n(T)}$ (11)

The angular frequency is represented by ω = 2πf, "B" is a temperature-dependent parameter with the unit of conductivity (U-cm) 1, and "n" is a non-dimensional parameter having values ranging from 0 to 1.

For $CaBaCo_{2-x}Mn_xYb_yFe_{12-y}O_{22}$ nano- ferrites, Fig. 11 illustrates the influence of Mn-Yb on ac in the frequency range 1 MHz – 3 GHz at room temperature. It indicates that the value of ac conductivity increases with the increased frequency within the low-frequency zone for all concentrations of the doping element Mn-Yb. The dispersion phenomena, on the other hand, developed in the higher frequency area. The occurrence of interfacial polarisation in ferrites is due to the heterogeneous polycrystalline structure. The boundary of ferrite material is divided up into high conductivity phases (grains) and low conductivity

matrix, according to Koop's phenomenological theory as well as the Maxwell-Wagner model (grain boundaries). Conduction and polarisation mechanisms are the same as in ferrites.

Three frequency areas were defined by the hopping model. First in the low-frequency zone, where transport takes place infinite pathways and conductivity is unaffected by frequency. In the second frequency range, transport is only possible with the inclusion of hopping infinite clusters, and conductivity increases as frequency increases. Third, high frequencies involving cutoff begin to introduce a prominent role in the conduction mechanism, which was stated in terms of the electron hopping model (Heikes & Johnson). The equation was used to compute the AC conductivity (σ_{ac}) of all clean and doped materials [31, 49].

$\sigma_{ac} = \omega\varepsilon_0\varepsilon'$ (12)

The association between lnf and log(σ_{ac}) for $CaBaCo_{2-x}Mn_xYb_yFe_{12-y}O_{22}$ nanoparticles is shown in Fig. 12. The following empirical relationship was used to determine AC conductivity (σ_{ac}).

$\sigma_{ac} = \omega\varepsilon_0\varepsilon' = \omega\varepsilon_0\varepsilon\tan\delta = 2\pi f \tan\delta$ (13)

This relationship establishes that ac conductivity (σ_{ac}) rises as frequency rises. We can calculate the slope (n) by plotting logσac vs logω as a function of Manganese-ytterbium concentration on a graph.

$\sigma_{ac} = B\omega^n + A\omega^n$ (14)

This relationship illustrates a straight line with slope n and an intercept logB at logω = 0 (also A = B are the same constants with the same conductivity unit) [52, 54].

3.4.5 Electric modulus

The fluctuation of both the real and imaginary parts of electric modulus against frequency is seen in Figs. 13 and 14. The electric modulus formalism is a powerful tool for understanding electrical transport processes including charge carrier hopping rates, conductivity relaxation time, and dielectric materials. If the region of grain boundaries covers a large volume in a heterogeneous system, the electric modulus formalism helps to explain semi-circles in Cole-Cole plots. The relaxation process happened with the change in frequency within Mn–Yb replaced $CaBaCo_{2-x}Mn_xYb_yFe_{12-y}O_{22}$ (where x = 0.00 to 1.0 and y = 0.00 to 0.1) hexaferrites evidenced by the formation of loss peaks in imaginary parts of electric modulus against frequency for the current examined samples. When the jumping frequency of charge carriers approaches that of the externally applied AC field, the peak is detected [57, 58]. The real (M') and imaginary (M") parts of the electric modulus are calculated from the real (ε') and imaginary (ε") parts of the dielectric constant using the following relationships:

$M = 1/\ ^*=1/(\ '+\ '') = M'+jM''$ (15)

Where

$M'=\ '/\{(\ ')^2 + (\ '')^2\}$ (16)

M"= "/ {(') ^{2} + (") ^{2}} (16)

The plot of the real part (M') indicates a constant increase in the magnitude of M' concerning frequency; nevertheless, due to the mobility of charge carriers in the short range, it reaches its maximum value. M' decreases initially and subsequently increases when the replacement level of Mn–Yb increases, displaying the opposite behavior of the dielectric constant.

Furthermore, M" begins to diminish in the low-frequency range. The frequency of oscillating dipoles approaches that of the applied AC field frequency at above 2 GHz, where the frequency of oscillating dipoles approaches that of the applied AC field frequency. The frequency region is determined by the relaxation peak's left region (low-frequency area). The Maxwell–Wagner model can be used to predict the behavior of complex conductivity in heterogeneous systems with two or more phases [59–61]. The electrons travel great distances (charge carriers hopping between neighboring locations). The right side of the relaxation peak, on the other hand, defines the frequency range in which charge carriers are mobile across small distances (i.e., they are constrained to their potential wells) [62, 63]. With the increase in frequency, the conversion from long-range to the short-range motion of charge carriers is specified by the frequency area where the relaxation peak arises.

3.4.6 Quality factor

The variation in Q values concerning applied frequency for Mn-Yb doped $CaBaCo_{2-x}Mn_xYb_yFe_{12-y}O_{22}$ hexaferrites is shown in Fig. 15. Quality factor (Q) initially exhibited an upward trend However; there is a downward tendency in the quality component. This diminishing tendency after reaching specific temperature limits is a feature of the formation of the pores formed inside the grains, which are developed at a very high frequency. As a result, the loss factor increases as a result of these pores and the Q value decreases. The highest Q-factor value was found in the high-frequency zone. The plot indicates that the quality factor values for all the prepared samples exhibit anomalous behavior above 2 GHz frequency. Dielectric properties like dielectric constant ('), dielectric loss ("), and tangent loss (Tanδ) are incompatible with one another. The fact that these ferrite substances have higher Q values and a resonance frequency exceeding 2 GHz suggest that they can be employed in high-frequency multilayer chip inductors. The ferrite materials' higher Q values make them a good choice for possible uses in high-frequency electronics devices such as resonators and high-frequency filters The synthesized hexaferrites can be used in high-frequency MLCIs due to their high-quality factor values as well as resonance frequency exceeding 2.0 GHz. [54, 64]

3.5 Magnetic properties

The M-H loops for all of the $CaBaCo_{2-x}Mn_xYb_yFe_{12-y}O_{22}$ where x = 0.00 to 1.0 and y = 0.00 to 0.1 hexagonal ferrites samples observed at a 20 kOe applied field are presented in Fig. 16. Magnetic hysteresis loops can be seen in all of the materials, indicating substantial ferromagnetic activity. Figure 17 depicts the fluctuation of saturation, remanence magnetization, as well as coercivity increasing dopant Mn concentration. It is clear that the significance of saturation magnetization improves at low doping levels and then switches as the doped level increases. Greater saturation magnetization values are

obtained for x 0.0, y = 0.0 doping concentration owing to the excessive magnetic moment of Mn (5mB) in comparison to Co_2 (3mB), resulting in increased accumulative spins along the c axis. It is due to the availability of divalent Mn ions that the magnetic characteristics of ferrite can be tailored to meet the needs of certain use. This behavior can be explained by two factors: (1) site preference, and (2) the parent and replaced ions' ionic radii. It is known that more electronegative ions preferentially occupy the octahedral coordination. Tetrahedral sites are preferred by ions with d1, d2, d3, and d4 orbitals, whereas ions with d6, d7, d8, and d9 orbitals prefer octahedral sites, and ions with d0, d5, and d10 orbitals have no preference [65]. Co ions tend to occupy the octahedral sites because they have a higher electronegativity value and a d7 orbital shape. Due to their d5 orbital shape, Mn ions, on the other hand, have no site preferences.

Magnetic characteristics such as saturation magnetization, remanence magnetization, as well as coercivity are all affected significantly. The ability to occupy a certain site is also influenced by the ions as well as their partner cation ionic radii. Because the ionic radii of Mn^{2+} and Co^{2+} are not equivalent in size, local strain is introduced, resulting in disorder to modification of local electronic states. This tendency in saturation, as well as remanence magnetization, has been noted by several researchers. As a result, Mn initially replaces Co at octahedral sites, resulting in an increase in net magnetization among tetrahedral and octahedral lattice sites. However, at greater dopant concentration, Mn tends to migrate to tetrahedral sites and displace Fe, lowering Fe^{3+} concentration, as a result of the buffering reaction.

$Fe^{3+} + Mn^{2+} \rightarrow Mn^{3+} + Fe^{2+}$

This substitution decreases Fe's magnetic moments, weakening the super-exchange interaction among octahedral and tetrahedral lattice sites. The lattice parameters (a and c) increase as x increases, increasing the distance between Fe and O and decreasing the Fe^{3+}-O-Fe^{3+} super-exchange interaction between both sublattices. Figure 16M-H loop of $CaBaCo_{2-x}Mn_xYb_yFe_{12-y}O_{22}$ where x = 0.00 to 1.0 and y = 0.00 to 0.1 hexagonal ferrites samples. As a result, with larger levels of x, the saturation magnetization of substituted hexaferrites diminishes.

The formula for calculating the Bohr magnetron number for $CaBaCo_{2-x}Mn_xYb_yFe_{12-y}O_{22}$ is

nB = (M * Ms)/5585 (17)

Where Ms is just the saturation magnetization in emu/g and M is the material's molecular weight. It is vital to note that saturation magnetization is an important parameter for Bohr magnetron calculations, and it is not saturated for current nanoparticles under the applied field of 20 kOe. As a result, it is critical to study it first using the law of approach to saturation [66] and the following formula:

$M = Ms (1- a/H - b/H^2) + {}_{hf}H$ (18)

The high field susceptibility parameter is $_{hf}$ and the anisotropy parameter is b. b can be stated as $b = Ha^2/15 = 4K_1^2\ 2/15M_5^2$ for hexagonal crystal structure, where H_a is the anisotropy field and K1 is the

anisotropy constant. Figure 17 shows variation in saturation magnetization (Ms) and Retentivity (M_r) of Mn-Yb substituted $CaBaCo_{2-x}Mn_xYb_yFe_{12-y}O^{22}$ (x = 0.0e0.9) hexaferrites system.

The experimental case's insufficient field, which is insufficient to align all the randomly oriented magnetic moments in the applied field direction, is attributed to the observed disparity in the estimated and calculated values of saturation magnetization. In the theoretical scenario, a finite field is used to orient all of the magnetic moments in the direction of the external field to achieve maximum saturation magnetization. After obtaining estimated saturation magnetization values, the Bohr magnetron number was determined using Eq. 17.

Another fundamental parameter, squareness or remnant ratio (S = Mr/Ms), is used to determine the magnetic hardness of the material, which is affected by the system's anisotropy. The quantity of squareness that fluctuates from 0 to 1 determines the presence or absence of distinct types of inter-grain group exchanges. Large values of S (0.5 < Mr/Ms < 1) indicate that the material is much more anisotropic, rigid, and single domain, according to Day et al research's which is known as the Day diagram. They also stated that 0.05 Mr/Ms 0.5 is for particles with a pseudo-single domain that interact via magnetostatic couplings, whereas Mr/Ms > 0.05 is for randomly oriented multi-domain nanoparticles [67]. Table 2 shows the squareness ratios (S) of Mn substituted $CaBaCo_{2-x}Mn_xYb_yFe_{12-y}O_{22}$ (x = 0.0–1, y = 0.0-0.1) hexaferrites. The squareness values for the samples under investigation range from 0.583 to 0.552, showing that the nanoparticles' nature is changing from pseudo-single domains to single domains. The coercivity, which is influenced by dopant concentration, is a measurement of the magnetic field intensity required to overcome magnetocrystalline anisotropy. The variation in coercivity and Mr/Ms of Mn-Yb doped Co2 Y-type barium hexagonal ferrites as a function of x is shown in Fig. 18.

Table 2
Various magnetic parameters of CaBaCo2-xMnxYbyFe12-yO22 where x = 0.00 to 1.0 and y = 0.00 to 0.1 hexagonal ferrites samples.

Compositions	Magnetization M_s (emu/g)	Retentivity M_r (emu/g)	M_r/M_s	H_c (O_e)
x = 0.0, y = 0.0	4.11	2.33	0.567	1776.78
x = 0.4, y = 0.04	2.64	1,54	0.583	1842.04
x = 0.8, y = 0.08	2.21	1.22	0.552	2283.51

With increasing dopant concentration, the diameter of the hysteresis loop for doping concentration grows. The value of coercivity rises dramatically from 1776.78 Oe to 2283.55Oe as Mn concentration rises from x = 0 to x = 0.9. The rationale for this rise in coercivity is as follows. With increasing doping concentrations, the porosity of the specimens rises, according to XRD calculations. Kersten and Neel suggested an interesting linear relationship between porosity and coercivity [23, 68].

In a ferromagnetic material, domain walls should ideally extend from pore to pore, according to their beliefs. It is widely thought that the sintering process leaves a certain quantity of air pores in polycrystalline sintered ferrites. Domain walls will extend from pore to pore in such porous structures and will not be able to move freely as they do in metals. Dependent on the quantity of porosity as well as the average diameter of pores in comparison to the wall thickness, irreversible domain wall displacements can develop in ferrites. As a result, it can be stated that coercivity in ferrites is heavily influenced by pores. This linear relationship can be explained by the presence of microscopic particles (perhaps in the single domain regime) in specimens with high porosity values, which raises the sample's coercivity. Similar results have been reported by Economos, who found that coercivity in Mg ferrites diminishes as porosity values drop [69]. If the coercivity is high enough above 1.2 kOe, hexaferrites materials can be used in a perpendicular recording medium (PRM), which is a new approach in magnetic recording media Furthermore, if Hc > Mr/2, the materials are hard magnets, which could be beneficial for high-frequency uses, according to If Hc < Mr/2, the materials are magnetically semi-hard and are employed in information storage. Because all of the produced hexaferrites materials in this investigation had Hc > Mr/2, they could be useful for high-frequency uses.[23, 70]

Conclusions

The influence of Mn^{2+}- Yb^{3+} substitution on the structural and dielectric and magnetic properties of $CaBaCo_{2-x}Mn_xYb_yFe_{12-y}O_{22}$ Y-type hexaferrites was investigated in this study. Sintering at a temperature of 1050^oC yielded single-phase Y-type compounds using the sol-gel technique. The XRD technique was used to validate the presence of pure Y-type structure as well as acquire information on lattice characteristics. Mn–Yb in the Y-type lattice enhanced crystallite size as well as increasing lattice constants (a, c), bulk density, and X-ray density. The tetrahedral and octahedral sites inherent vibrational bands migrated to the lower frequency side owing to the presence of Mn–Yb ions. The production of hexaferrites is confirmed by FTIR analysis. The typical ferrite dielectric response was seen in dielectric parameters, which were completely characterized in light of Koop's and Maxwell's theories and Wagner's by considering the hopping process. The dielectric constant, ac conductivity, and Q-factor values were improved when Mn–Yb was substituted. From the M-H hysteresis loop of the VSM, magnetic characteristics such as coercivity, saturation magnetization, squareness ratio, and retentivity were obtained. With good remnant and saturation magnetization, as well as a high squareness ratio, the coercivity values were found to be the highest, indicating that Mn^{2+}-Yb^{3+} doping can significantly improve the magnetic properties of Co_2-Y ferrite for magnetic uses such as permanent magnets, magnetic data storage devices, and magnetic tapes.

Declarations

Declaration of competing interest

There is no conflict of interest on the manuscript entitled "**Enhanced Structural, Dielectric, and Magnetic Properties of Mn-Yb-doped Y-type Hexaferrites**" to the best of our knowledge and belief.

Author contributions

Muhammad Nadeem: Synthesis, Characterization, Writing-original draft, Writing - review & editing. **Dr Hasan Mehmood khan**: Supervision, Methodology, Software, Resources, Investigation and Validation, Reviewing and Editing. **Saeed Ahmad Buzdar**: Co-supervision. **Javed Ahmed, Mohammad A. Assiri and Muhammad Imran**: Synthesis and Characterization. **Ambreen Aleem**: Visualization XRD and FTIR Results Analysis. **Mohammad Ehsan Raza and Mehrun Nisa**: Dielectric properties data analysis.**:** Magnetic Parameters.

Data availability statement

The data that supporting findings of this study are available upon reasonable request from the authors

Acknowledgement

The authors **Muhammad Nadeem** and **Dr Hasan Mehmood Khan** are thankful to Higher Education Commission (HEC) of Pakistan and The Islamia University of Bahawalpur-Pakistan

References

1. J. Mohammed et al., Effect of Cr–Bi substitution on the structural, optical, electrical and magnetic properties of strontium hexaferrites. Phys. B: Condens. Matter **575**, 411681 (2019)
2. J. Mohammed et al., Lightweight SrM/CCTO/rGO nanocomposites for optoelectronics and Ku band microwave absorption. J. Mater. Sci.: Mater. Electron. **30**(4), 4026–4040 (2019)
3. T. Tchouank Tekou Carol et al., X-band shielding of electromagnetic interference (EMI) by Co 2 Y barium hexaferrite, bismuth copper titanate (BCTO), and polyaniline (PANI) composite. J. Magn. Magn. Mater. **501**, 166433 (2020)
4. I. Auwal et al., Structural, magneto-optical properties and cation distribution of SrBixLaxYxFe12 – 3xO19 ($0.0 \leq x \leq 0.33$) hexaferrites. Mater. Res. Bull. **80**, 263–272 (2016)
5. T.T.T. Carol et al., X-band shielding of electromagnetic interference (EMI) by Co2Y barium hexaferrite, bismuth copper titanate (BCTO), and polyaniline (PANI) composite. J. Magn. Magn. Mater. **501**, 166433 (2020)
6. J. Mohammed et al., Crystal structure refinement and the magnetic and electro-optical properties of Er3+–Mn2+-substituted Y-type barium hexaferrites. Ceram. Int. **47**(13), 18455–18465 (2021)
7. I. Mohammed et al., *Influence of Mn2+-substitution on the structural, morphological and magnetic properties of Co2Y strontium hexaferrites.* Materials Today: Proceedings, 2022
8. I. Ali et al., Synthesis and magnetic properties of (Eu–Ni) substituted Y-type hexaferrite by surfactant assisted co-precipitation method. J. Magn. Magn. Mater. **385**, 386–393 (2015)

9. J.-H. You, S.-I. Yoo, Magnetic properties of Zn-substituted Y-type hexaferrites, Ba2ZnxFe2 – xFe12O22. J. Magn. Magn. Mater. **471**, 255–261 (2019)
10. M. Nadeem et al., Structural, dielectric, and magnetic properties of CaBaCo2-xZnxNdyFe12-yO22 Y-type hexaferrites. J. Mater. Sci.: Mater. Electron. **33**(9), 6294–6306 (2022)
11. M. Manendar et al., Cation distribution in Ni substituted Ba0. 5Sr1. 5Co2Fe12O22 Y-type hexagonal ferrites. Ceram. Int. **47**(7), 9591–9596 (2021)
12. L. Omari et al., Effect of low amount Mn doping on structural and magnetic properties of SrFe12O19: Effective magnetic anisotropy study by Stoner-Wohlfarth model. Mater. Today Commun. **27**, 102257 (2021)
13. C. Wang et al., *Magnetic field-induced polarization reversal in Y-type hexaferrites Ba0. 7 Sr1. 3CoZnFe11AlO22 single crystals.* Ceramics International, 2021. **47**(14): p. 19356–19361
14. R.C. Pullar, *Hexagonal ferrite fibres and nanofibres. in Solid State Phenomena* (Trans Tech Publ, 2016)
15. P. Hernández-Gómez et al., Broadband transverse susceptibility in multiferroic Y-type hexaferrite Ba0. 5Sr1. 5Co2Fe2O22. J. Magn. Magn. Mater. **476**, 478–482 (2019)
16. P. Behera, S. Ravi, Impedance spectroscopy and magnetic properties of Mg doped Y-type barium hexaferrite. J. Mater. Sci.: Mater. Electron. **29**(23), 20206–20215 (2018)
17. N.J. Vickers, Animal communication: when i'm calling you, will you answer too? Curr. Biol. **27**(14), R713–R715 (2017)
18. K. Zhai et al., Giant magnetoelectric effects achieved by tuning spin cone symmetry in Y-type hexaferrites. Nat. Commun. **8**(1), 1–8 (2017)
19. J. Mohammed et al., Crystal-structure analysis, Raman spectroscopy, dielectric measurements, magnetic and optical properties of Cr3+–Ni2+-substituted Co2Y-type barium hexaferrites. Mater. Res. Bull. **145**, 111564 (2022)
20. H. Khanduri et al., Structural, dielectric, magnetic, and nuclear magnetic resonance studies of multiferroic Y-type hexaferrites. J. Appl. Phys. **112**(7), 073903 (2012)
21. V.V. Warhate, D.S. Badwaik, Structural, magnetic and thermo-magnetic properties of NiMn Y-Type strontium nano-hexaferrites. J. Alloys Compd. **818**, 152830 (2020)
22. M. Junaid et al., Impact of Bi–Cr substitution on the structural, spectral, dielectric and magnetic properties of Y-type hexaferrites. Ceram. Int. **46**(16), 25478–25484 (2020)
23. N. Adeela et al., Structural and magnetic response of Mn substituted Co2 Y-type barium hexaferrites. J. Alloys Compd. **686**, 1017–1024 (2016)
24. B.D. Cullity, *Elements of X-ray Diffraction* (Addison-Wesley Publishing, 1956)
25. A. Elahi et al., Preparation and properties of sol–gel synthesized Mg-substituted Ni2Y hexagonal ferrites. Ceram. Int. **39**(2), 983–990 (2013)
26. S.H. Mahmood, Magnetic properties and hyperfine interactions in M-type BaFe12-2xMoxZnxO19 hexaferrites. J. Appl. Math. Phys. **2**(05), 77 (2014)

27. M. Salunkhe, D. Kulkarni, Structural, magnetic and microstructural study of Sr2Ni2Fe12O22. J. Magn. Magn. Mater. **279**(1), 64–68 (2004)
28. X. Zhong et al., Improving soft magnetic properties of Mn-Zn ferrite by rare earth ions doping. AIP Adv. **8**(4), 047807 (2018)
29. W.E. Lee, M. Rainforth, *Ceramic microstructures: property control by processing* (Springer Science & Business Media, 1994)
30. A. Majeed et al., Morphological, Raman, electrical and dielectric properties of rare earth doped X-type hexagonal ferrites. Phys. B: Condens. Matter **503**, 38–43 (2016)
31. I. Ali et al., Role of grain boundaries in the conduction of Eu–Ni substituted Y-type hexaferrites. J. Magn. Magn. Mater. **362**, 115–121 (2014)
32. A. Mali, A. Ataie, Influence of the metal nitrates to citric acid molar ratio on the combustion process and phase constitution of barium hexaferrite particles prepared by sol–gel combustion method. Ceram. Int. **30**(7), 1979–1983 (2004)
33. C. Zhang et al., Effects of calcination temperature and solution pH value on the structural and magnetic properties of Ba2Co2Fe12O22 ferrite via EDTA-complexing process. Mater. Chem. Phys. **123**(2–3), 551–556 (2010)
34. A. Aslam et al., High frequency electrical transport properties of CoFe2O4 and Sr2NiMnFe12O22 composite ferrites. Ceram. Int. **40**(1), 155–162 (2014)
35. M.J. Iqbal, Synthesis and study of physical properties of Zr4+–Co2 + co-doped barium hexagonal ferrites. Mater. Sci. Engineering: B **164**(1), 6–11 (2009)
36. M. Ahmad et al., Effects of divalent ions substitution on the microstructure, magnetic and electromagnetic parameters of Co2W hexagonal ferrites synthesized by sol–gel method. J. Alloys Compd. **579**, 57–64 (2013)
37. A. Nairan et al., Temperature-dependent magnetic response of antiferromagnetic doping in cobalt ferrite nanostructures. Nanomaterials **6**(4), 73 (2016)
38. I. Ali et al., Synthesis and characterization of hexagonal ferrite Co2Sr2Fe12O22 with doped polypyrrole composites. Curr. Appl. Phys. **13**(6), 1090–1095 (2013)
39. D. Ramimoghadam, S. Bagheri, S.B. Abd Hamid, Progress in electrochemical synthesis of magnetic iron oxide nanoparticles. J. Magn. Magn. Mater. **368**, 207–229 (2014)
40. M.V. Rane et al., Magnetic properties of NiZr substituted barium ferrite. J. Magn. Magn. Mater. **195**(2), L256–L260 (1999)
41. S. Hussain, A. Maqsood, Influence of sintering time on structural, magnetic and electrical properties of Si–Ca added Sr-hexa ferrites. J. Magn. Magn. Mater. **316**(1), 73–80 (2007)
42. Z. Anwar et al., Investigation of dielectric behavior of new Tb3 + doped BiFeO3 nanocrystals synthesized via micro-emuslion route. J. Ovonic Res. Vol **10**(6), 265–273 (2014)
43. M. Anis-ur-Rehman, G. Asghar, Variation in structural and dielectric properties of co-precipitated nanoparticles strontium ferrites due to value of pH. J. Alloys Compd. **509**(2), 435–439 (2011)

44. M.J. Iqbal, M.N. Ashiq, I.H. Gul, Physical, electrical and dielectric properties of Ca-substituted strontium hexaferrite (SrFe12O19) nanoparticles synthesized by co-precipitation method. J. Magn. Magn. Mater. **322**(13), 1720–1726 (2010)
45. I.M. Abdulmajeed, Dielectric Behavior of Nickel-Zinc Dopped Hexagonal W-type Barium Ferrite. Al-Nahrain J. Sci. **15**(2), 102–105 (2012)
46. T. Hussain et al., Induced modifications in the properties of Sr doped BiFeO3 multiferroics. Progress in Natural Science: Materials International **23**(5), 487–492 (2013)
47. M. Irfan et al., *Effect of Y2O3 doping on the electrical transport properties of Sr2MnNiFe12O22 Y-type hexaferrite.* Current Applied Physics, 2014. **14**(1): p. 112–117
48. I. Ali et al., Effect of Eu–Ni substitution on electrical and dielectric properties of Co–Sr–Y-type hexagonal ferrite. Mater. Res. Bull. **49**, 338–344 (2014)
49. M.A. Iqbal et al., High frequency dielectric properties of Eu + 3-substituted Li–Mg ferrites synthesized by sol–gel auto-combustion method. J. Alloys Compd. **586**, 404–410 (2014)
50. I. Sadiq et al., Structural, infrared, magnetic and microwave absorption properties of rare earth doped X-type hexagonal nanoferrites. J. Alloys Compd. **570**, 7–13 (2013)
51. A. Kagdi, R.B. Jotania, Structural and dielectric properties hexaferrite/poly (Vinyl Alcohol) composites. Res. Rev. : J. Phys. **2**, 10–19 (2014)
52. K.M. Batoo, Study of dielectric and impedance properties of Mn ferrites. Phys. B: Condens. Matter **406**(3), 382–387 (2011)
53. I. Sadiq et al., Influence of Nd-Co substitution on structural, electrical, and dielectric properties of x-type hexagonal nanoferrites. J. Mater. Eng. Perform. **23**(2), 622–627 (2014)
54. M.K. Sharif et al., Synthesis and characterization of Zr and Mg doped BiFeO3 nanocrystalline multiferroics via micro emulsion route. J. Alloys Compd. **667**, 329–340 (2016)
55. I. Gul, A. Maqsood, Structural, magnetic and electrical properties of cobalt ferrites prepared by the sol–gel route. J. Alloys Compd. **465**(1–2), 227–231 (2008)
56. A.A. El Ata et al., Studies of AC electrical conductivity and initial magnetic permeability of rare-earth-substituted Li–Co ferrites. J. Magn. Magn. Mater. **297**(1), 33–43 (2006)
57. A. Abdeen et al., Structural, electrical and transport phenomena of Co ferrite substituted by Cd. J. Magn. Magn. Mater. **238**(1), 75–83 (2002)
58. E. Pervaiz, I. Gul. *Influence of rare earth (Gd3+) on structural, gigahertz dielectric and magnetic studies of cobalt ferrite*. in *Journal of Physics: Conference Series*. 2013. IOP Publishing
59. E. Barsoukov, J.R. Macdonald, *Impedance Spectroscopy Theory, Experiment, and.* Applications, 2nd ed.(Hoboken, NJ: John Wiley &Sons, Inc., 2005), 2005
60. H. Rodrigues et al., BiFeO3 ceramic matrix with Bi2O3 or PbO added: Mössbauer, Raman and dielectric spectroscopy studies. Phys. B: Condens. Matter **406**(13), 2532–2539 (2011)
61. A. Bagum, M.B. Hossen, F.-U.-Z. Chowdhury, Complex impedance and electric modulus studies of Al substituted Co0. 4Cu0. 2Zn0. 4AlxFe2-xO4 ferrites prepared by auto combustion technique.

Ferroelectrics **494**(1), 19–32 (2016)

62. M.Y. Lodhi et al., Unveiling the effect of Gd–Co co-substitution in the enrichment of structural and dielectric properties of SrBaMn based magnetic oxide. Ceram. Int. **48**(6), 8612–8619 (2022)
63. R. Kausar et al., *Investigation into the structural and magnetic features of nickel doped U-type hexaferrites prepared through sol–gel method*. Journal of Magnetism and Magnetic Materials, 2022: p. 169054
64. F. ur Raheem et al., Structural, spectral, electrical, dielectric and magnetic properties of Yb doped SrNiCo-X hexagonal nano-structured ferrites. J. Alloys Compd. **708**, 903–910 (2017)
65. M.V. Rane et al., Mössbauer and FT-IR studies on non-stoichiometric barium hexaferrites. J. Magn. Magn. Mater. **192**(2), 288–296 (1999)
66. J. Singh et al., Elucidation of phase evolution, microstructural, Mössbauer and magnetic properties of Co2 + Al3 + doped M-type BaSr hexaferrites synthesized by a ceramic method. J. Alloys Compd. **695**, 1112–1121 (2017)
67. J. Roza et al., Paleomagnetic secular variation and environmental magnetism of Holocene-age sediments from Tulare Lake. *CA.* Quaternary Research **85**(3), 391–398 (2016)
68. M. Kersten, Zur Wirkung von Werkstoffverunreinigungen auf die Anfangspermeabilität. Z. für Phys. Chemie **198**(1), 89–106 (1951)
69. S. Blum, Microstructure and properties of ferrites. J. Am. Ceram. Soc. **41**(11), 489–493 (1958)
70. I. Ali et al., Effects of Ga–Cr substitution on structural and magnetic properties of hexaferrite (BaFe12O19) synthesized by sol–gel auto-combustion route. J. Alloys Compd. **547**, 118–125 (2013)

Figures

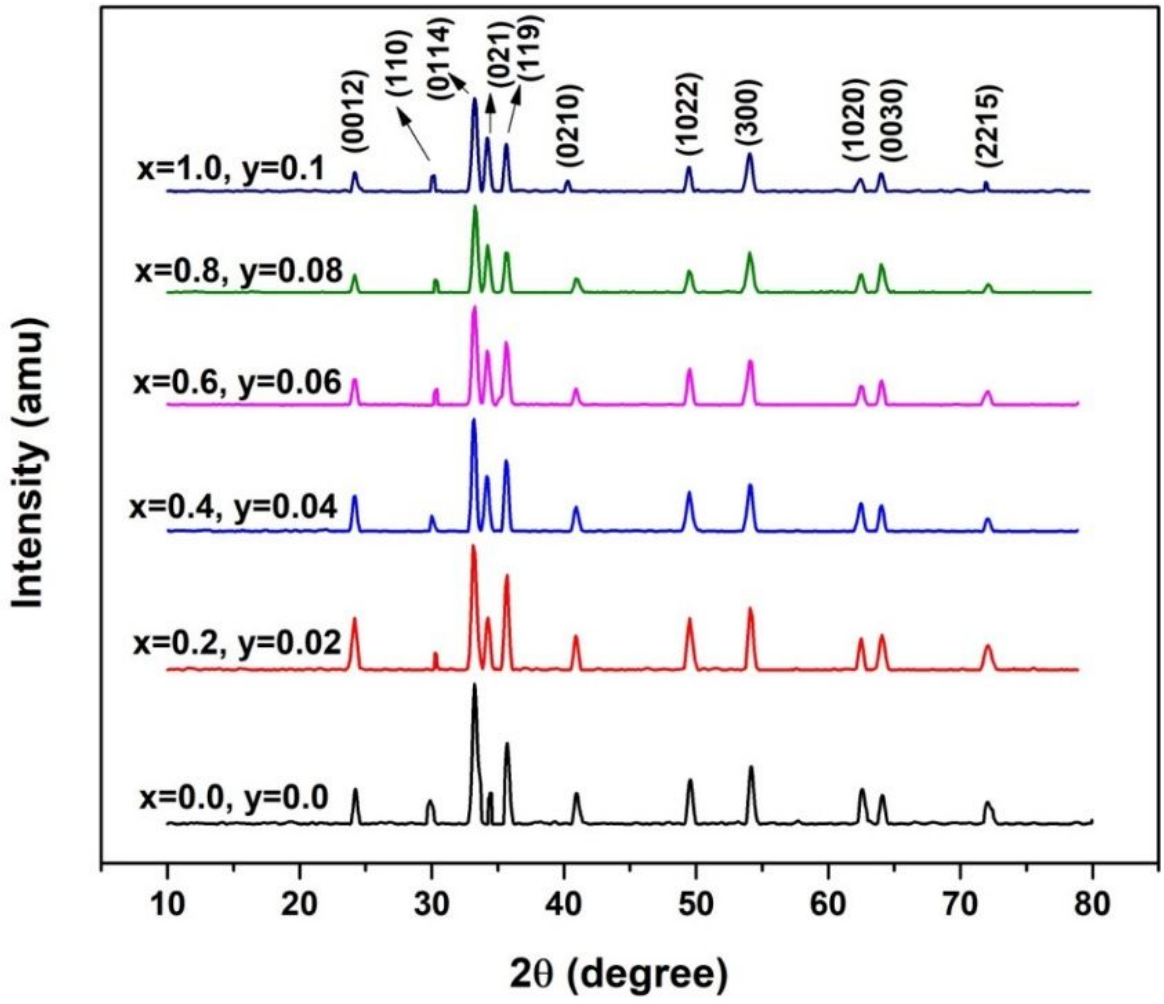

Figure 1

X-ray diffraction pattern for CaBaCo2-xMnxYbyFe12-yO22where x=0.00 to 1.0 and y=0.00 to 0.1 hexagonal ferrites.

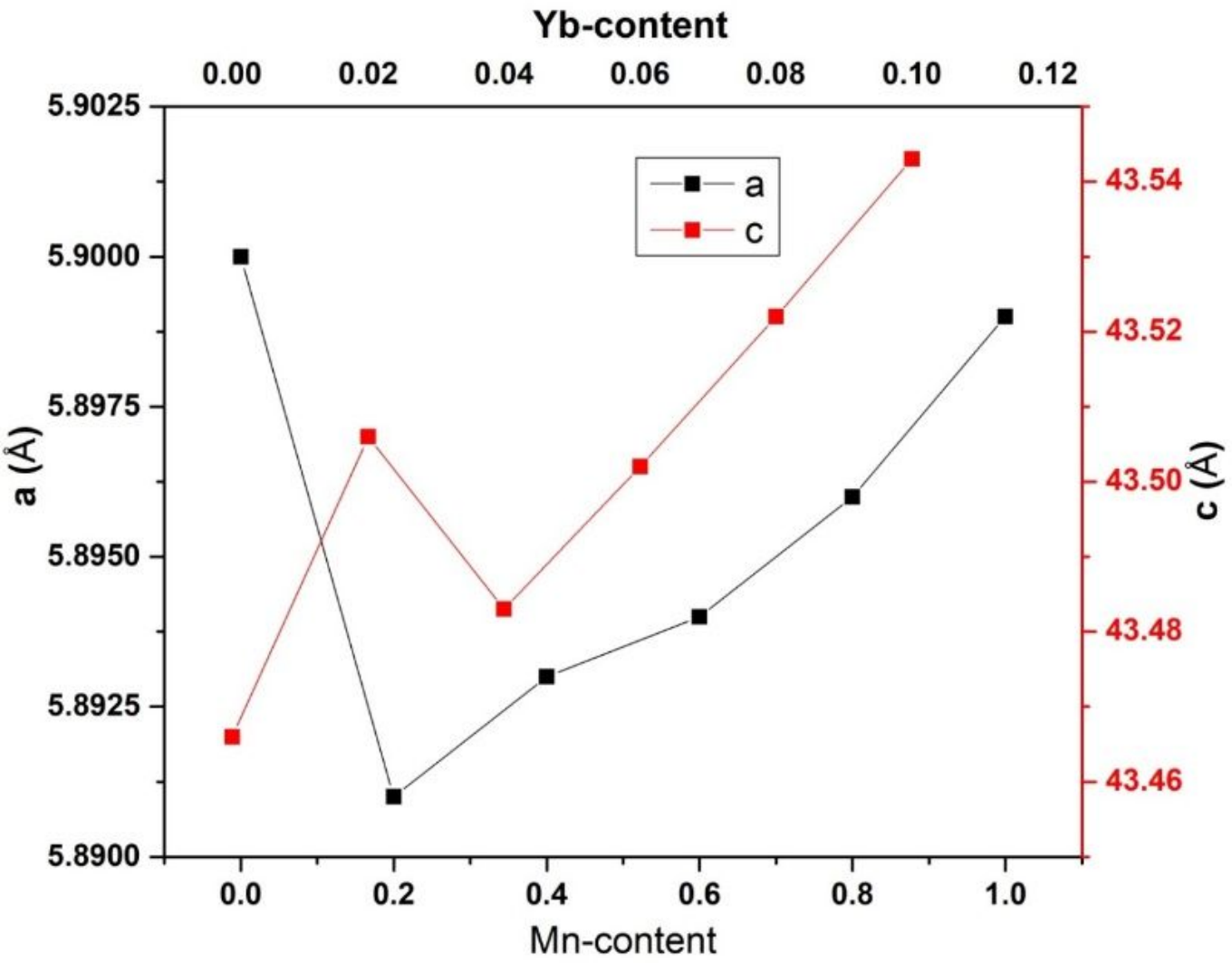

Figure 2

Variation of lattice parameters ‘a’ and ‘c’ for CaBaCo2-xMnxYbyFe12-yO22where x=0.00 to 1.0 and y=0.00 to 0.1 hexagonal ferrites.

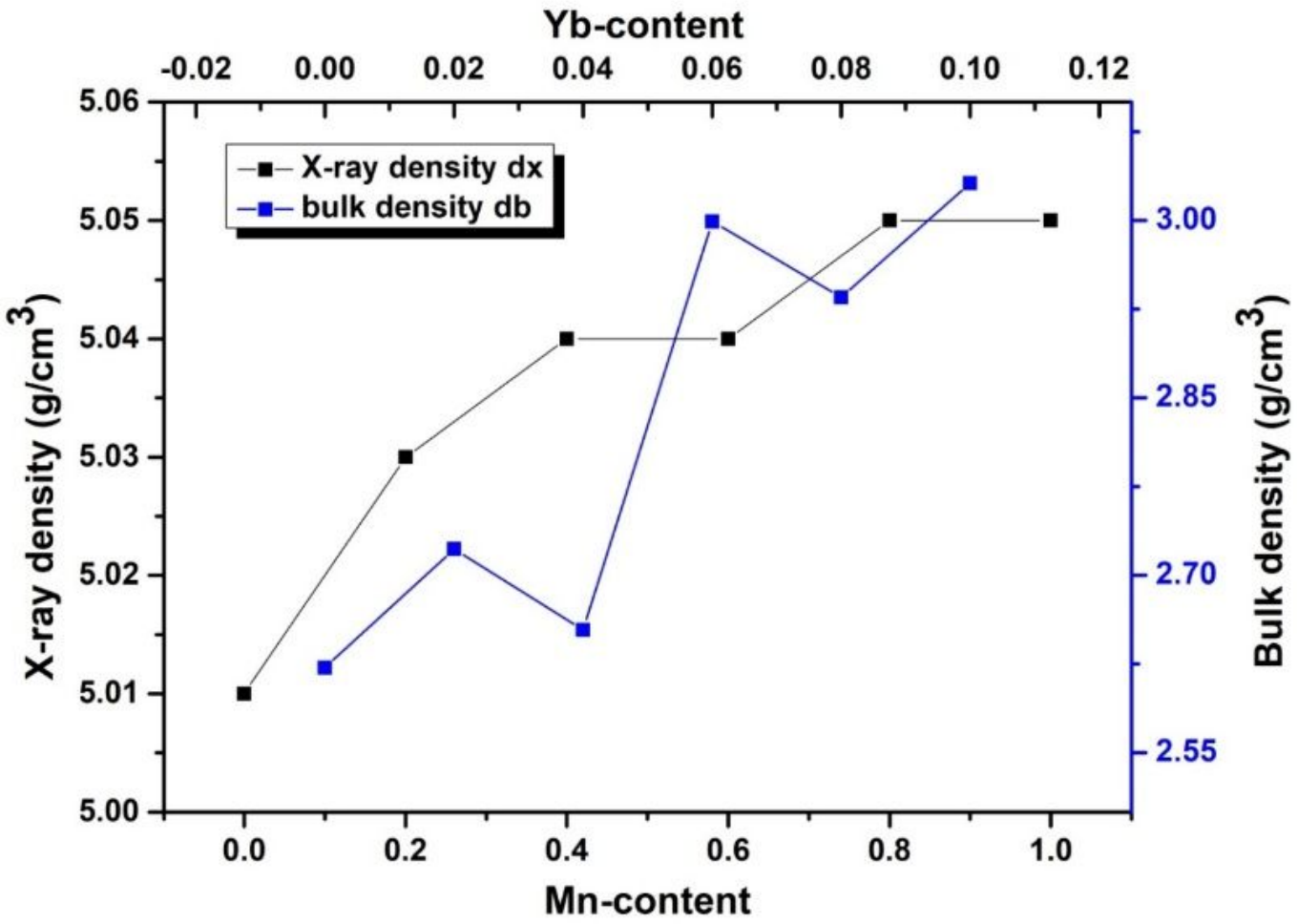

Figure 3

Variation in x-ray density (dx) and bulk density (db) for CaBaCo2-xMnxYbyFe12-yO22where x=0.00 to 1.0 and y=0.00 to 0.1 hexagonal ferrites.

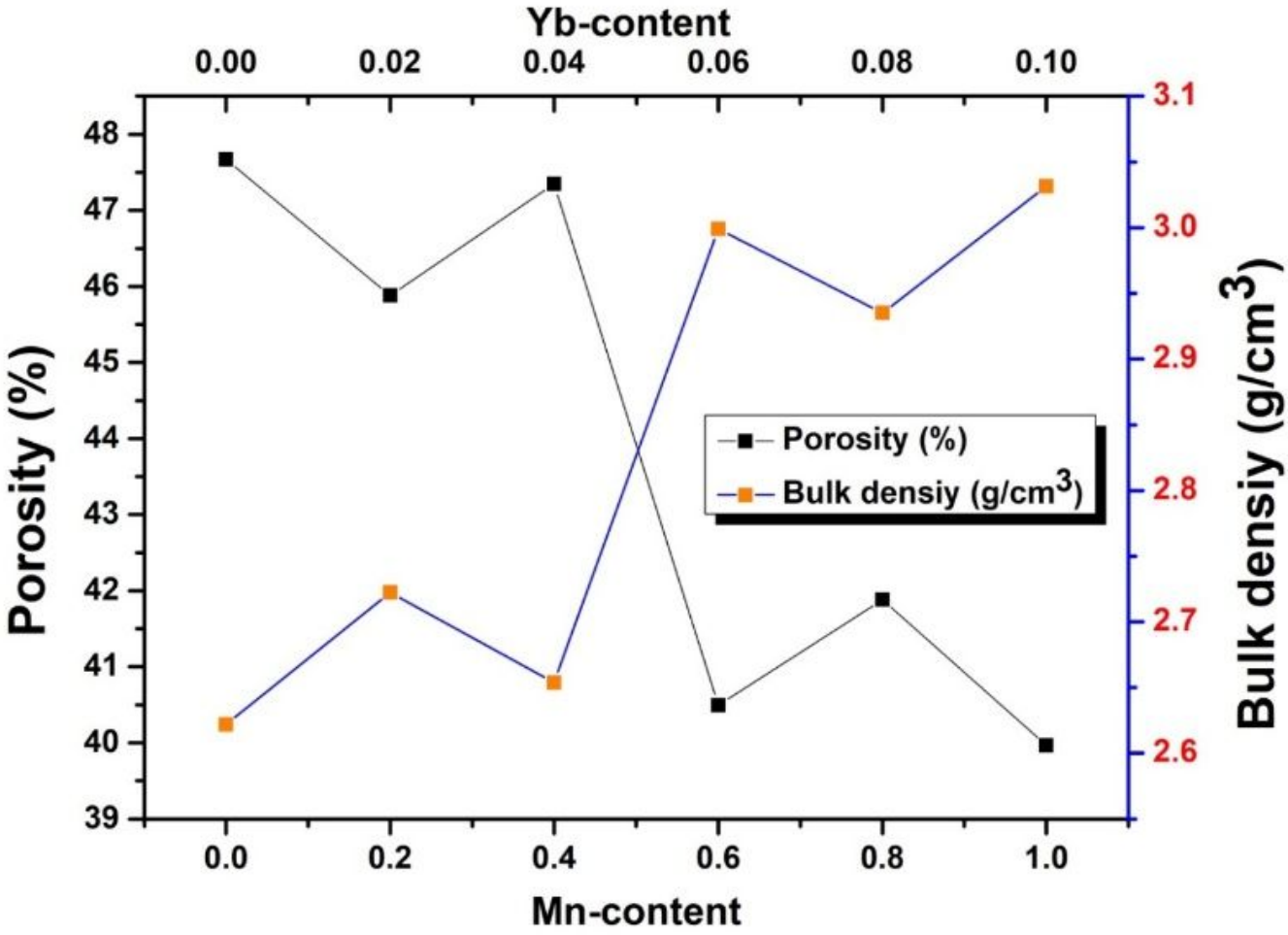

Figure 4

Variation in porosity (P) and bulk density (db) for CaBaCo2-xMnxYbyFe12-yO22 where x=0.00 to 1.0 and y=0.00 to 0.1 hexagonal ferrites.

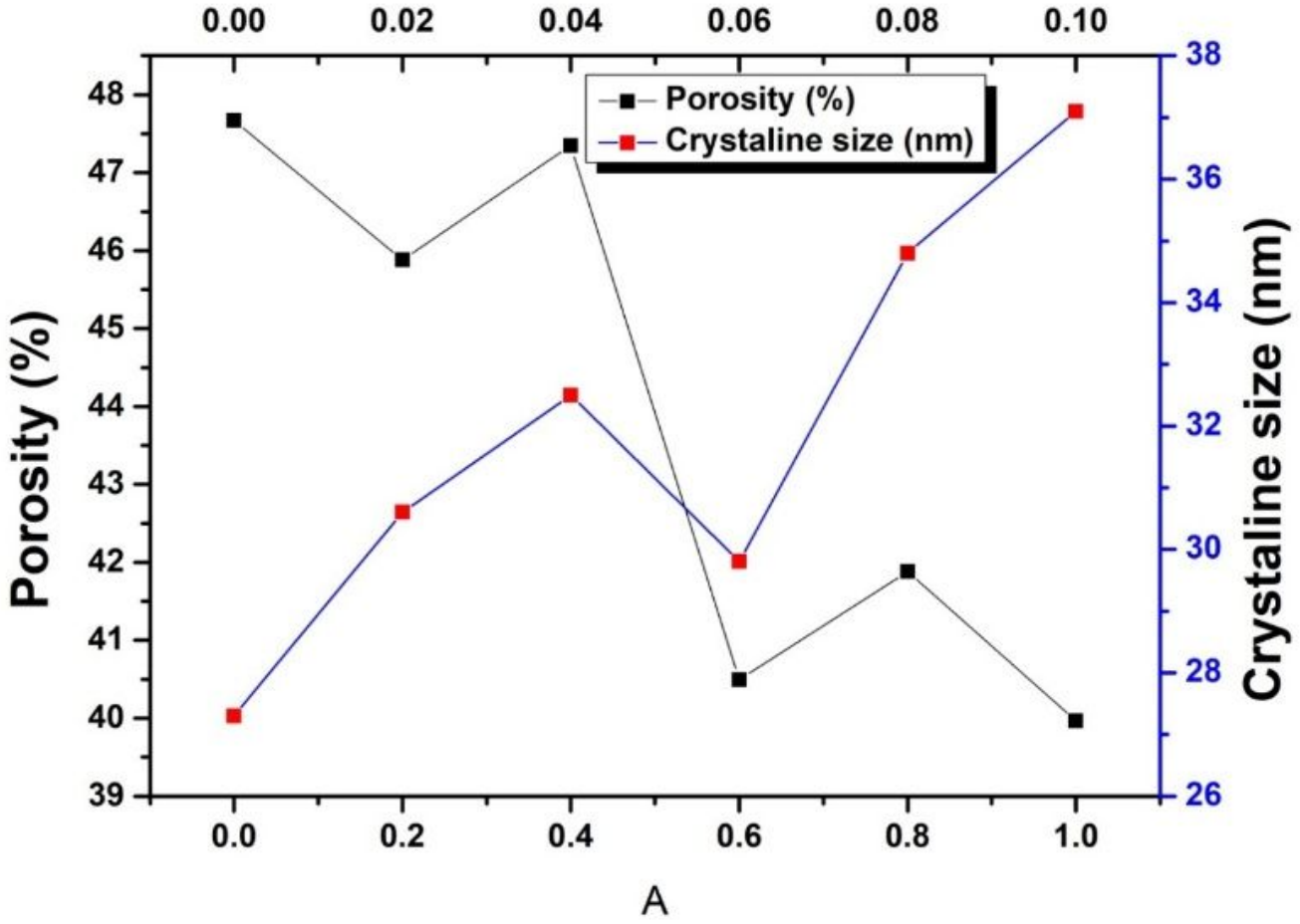

Figure 5

Variation in porosity (P) and crystalline size for CaBaCo2-xMnxYbyFe12-yO22where x=0.00 to 1.0 and y=0.00 to 0.1 hexagonal ferrites

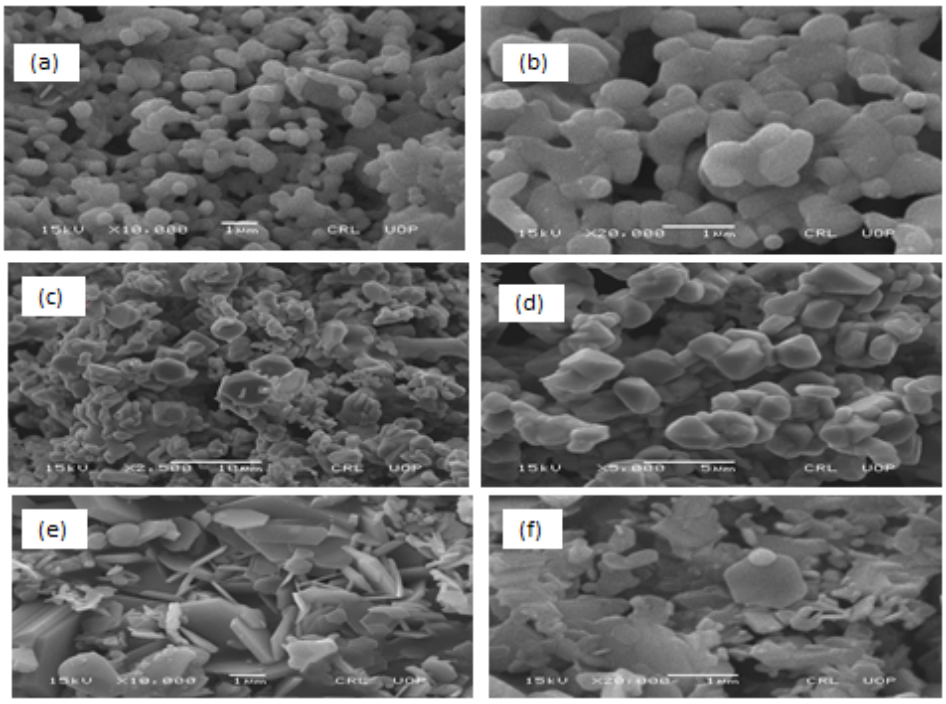

Figure 6

The SEM of CaBaCo2-xMnxYbyFe12-yO22where x=0.00 to 1.0 and y=0.00 to 0.1 hexagonal ferrites.

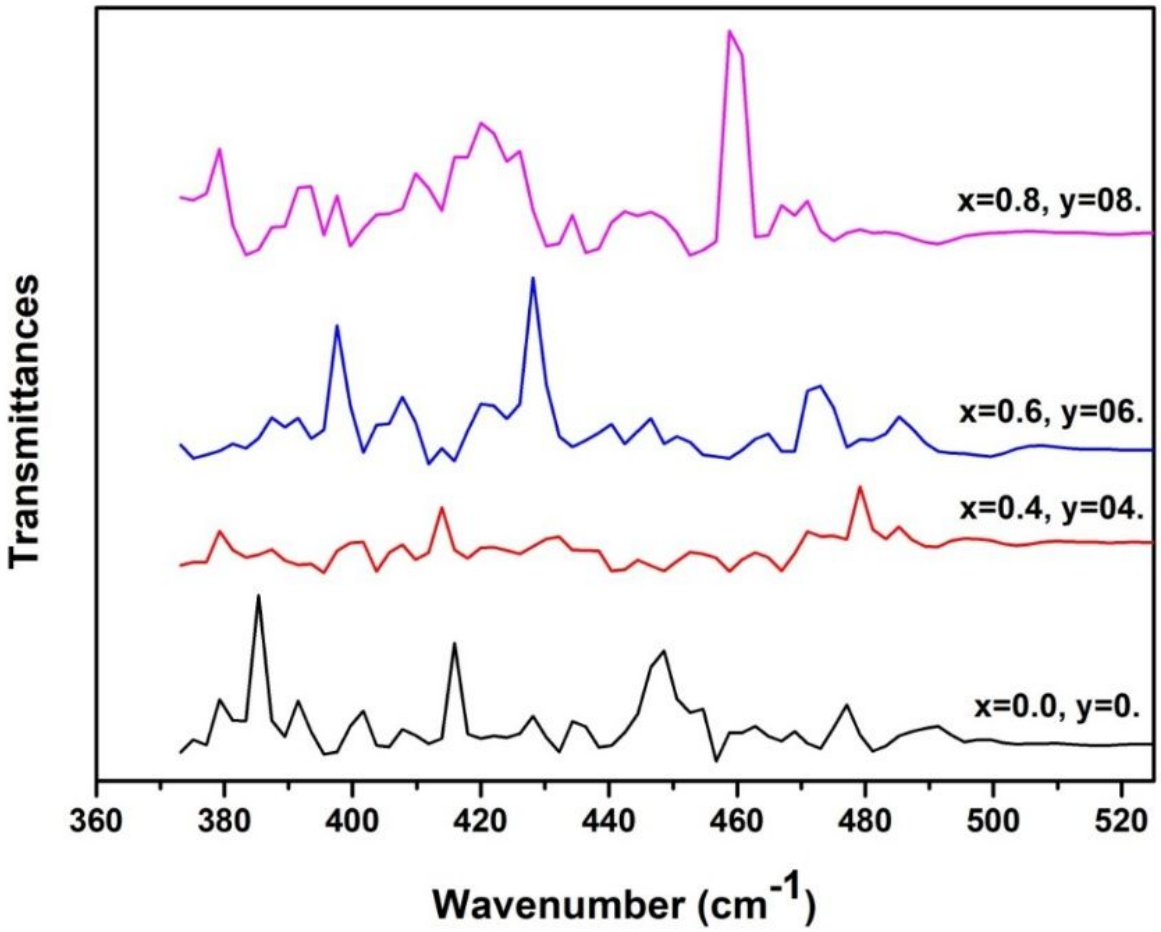

Figure 7

FTIR spectra of CaBaCo2-xMnxYbyFe12-yO22where x=0.00 to 1.0 and y=0.00 to 0.1 hexagonal ferrites.

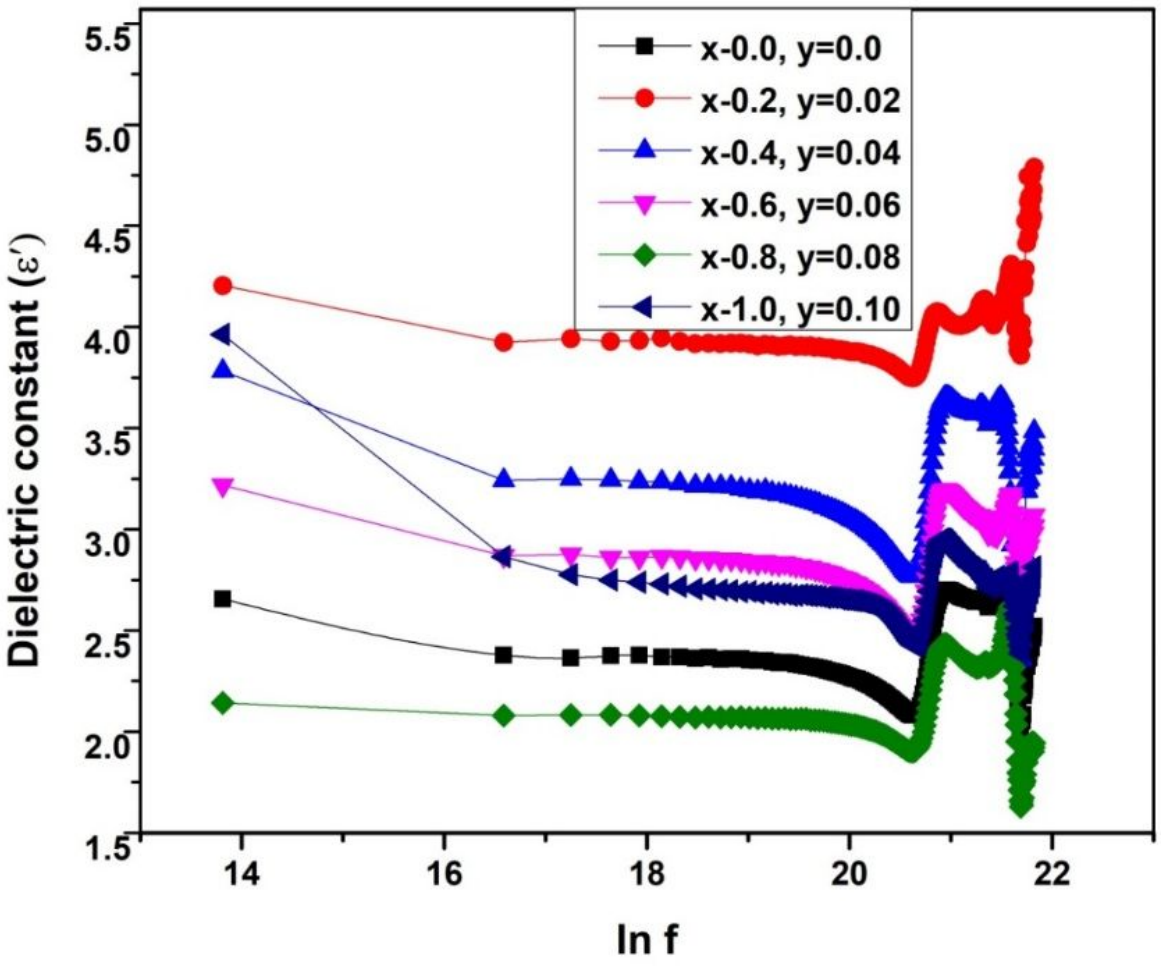

Figure 8

Dielectric constant (') as function of frequency for CaBaCo2-xMnxYbyFe12-yO22where x=0.00 to 1.0 and y=0.00 to 0.1 hexagonal ferrites.

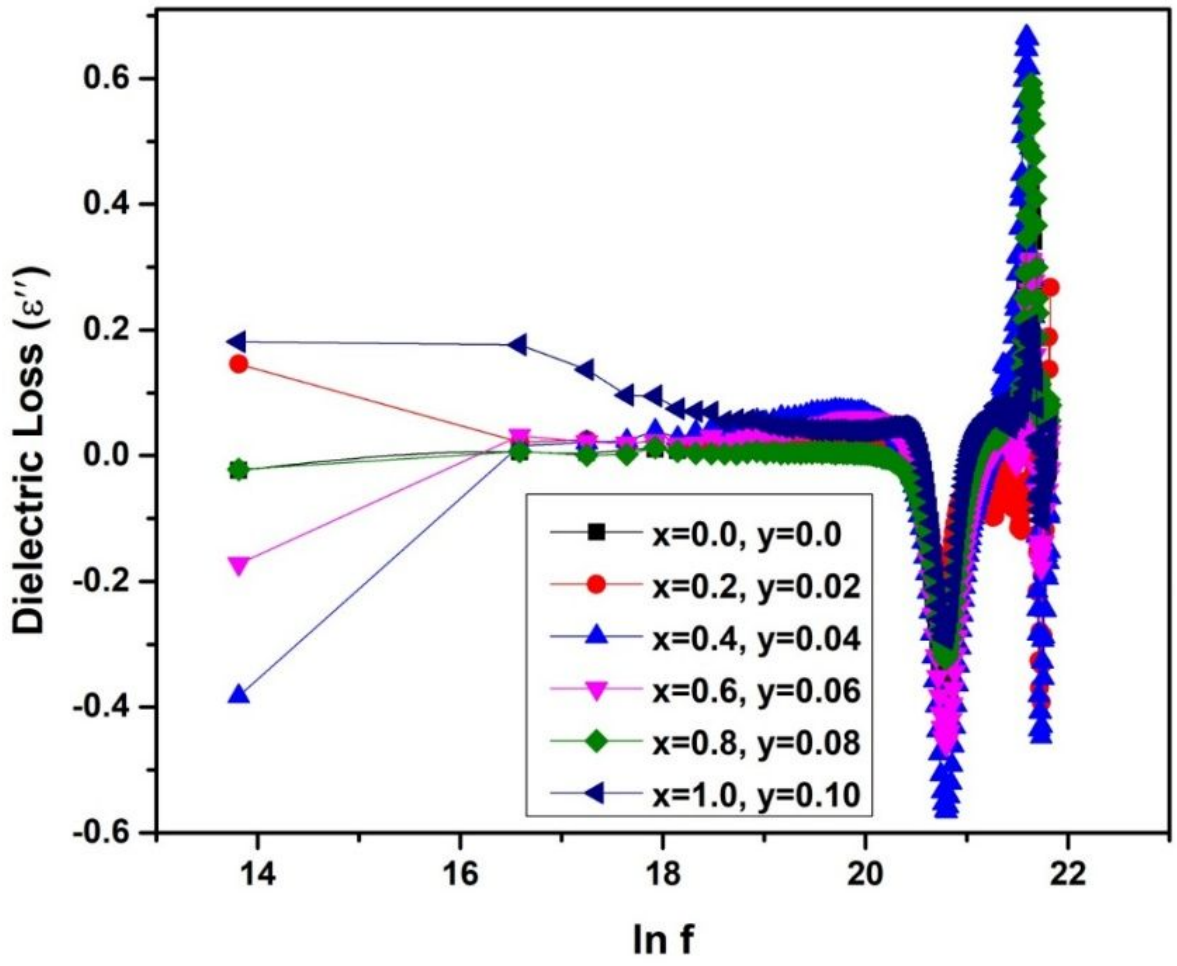

Figure 9

Dielectric loss ('') as function of frequency for CaBaCo2-xMnxYbyFe12-yO22where x=0.00 to 1.0 and y=0.00 to 0.1 hexagonal ferrites.

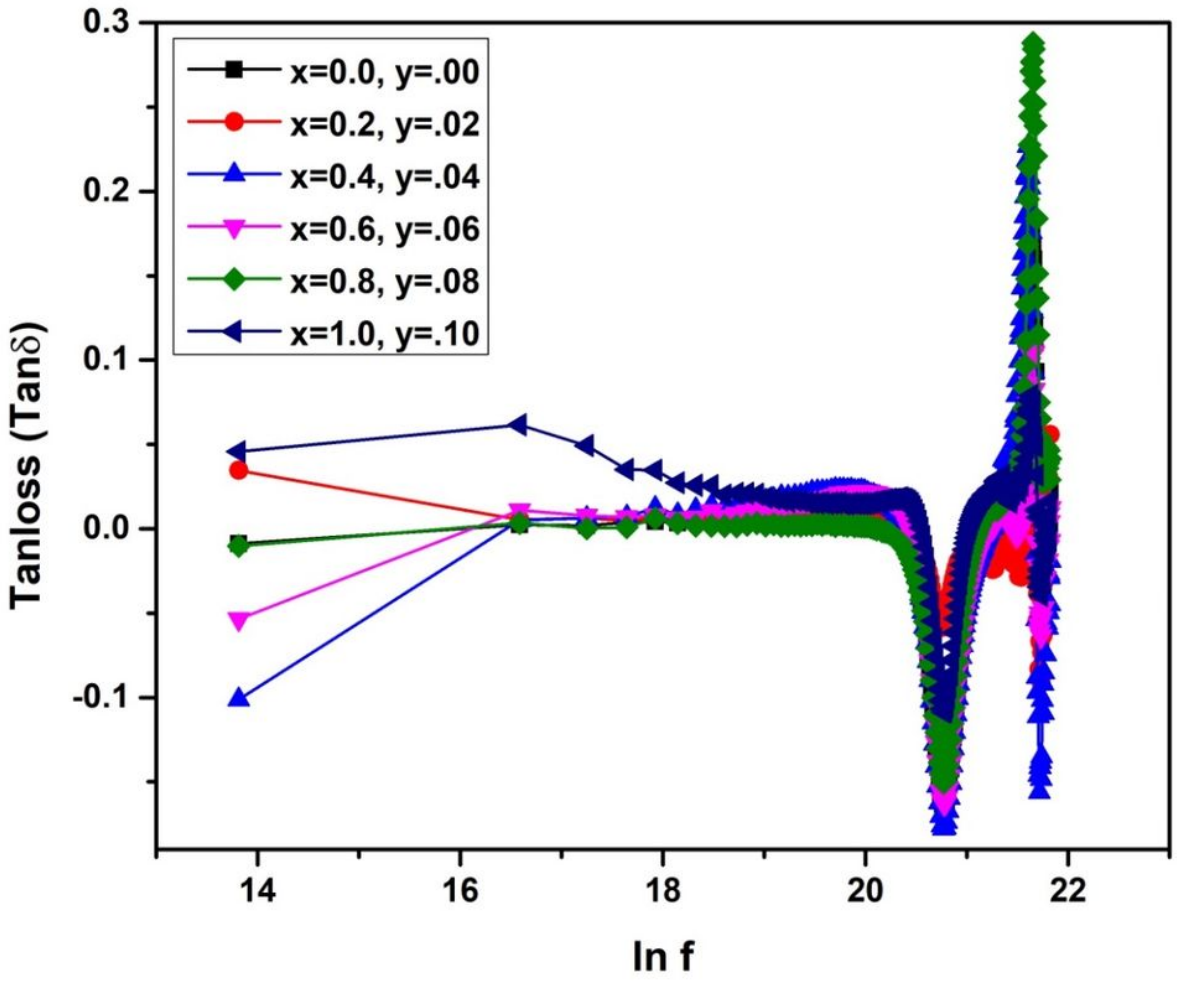

Figure 10

Tan loss (Tan δ) as function of frequency for CaBaCo2-xMnxYbyFe12-yO22where x=0.00 to 1.0 and y=0.00 to 0.1 hexagonal ferrites.

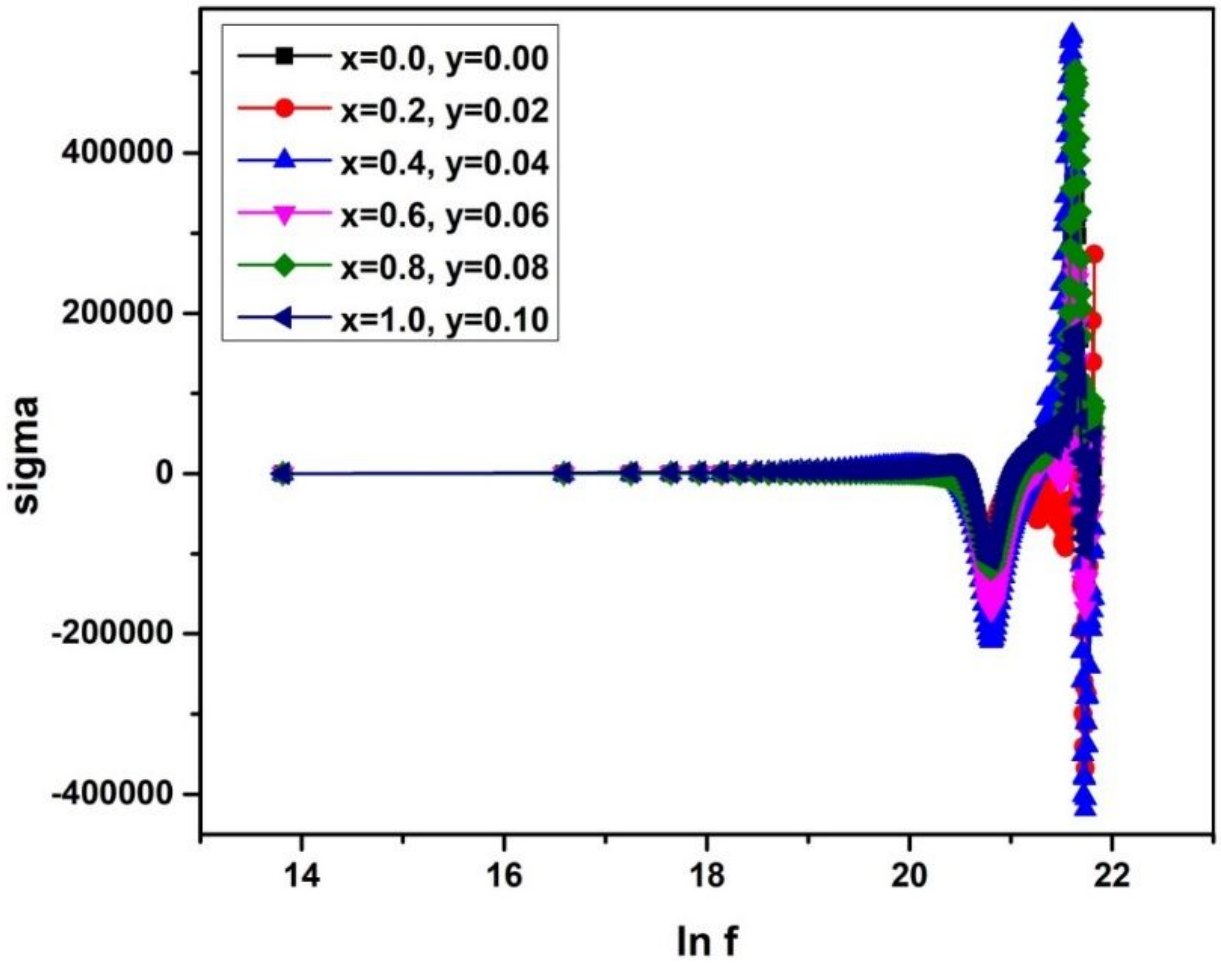

Figure 11

AC conductivity (σ ac) versus frequency for CaBaCo2-xMnxYbyFe12-yO22where x=0.00 to 1.0 and y=0.00 to 0.1 hexagonal ferrites.

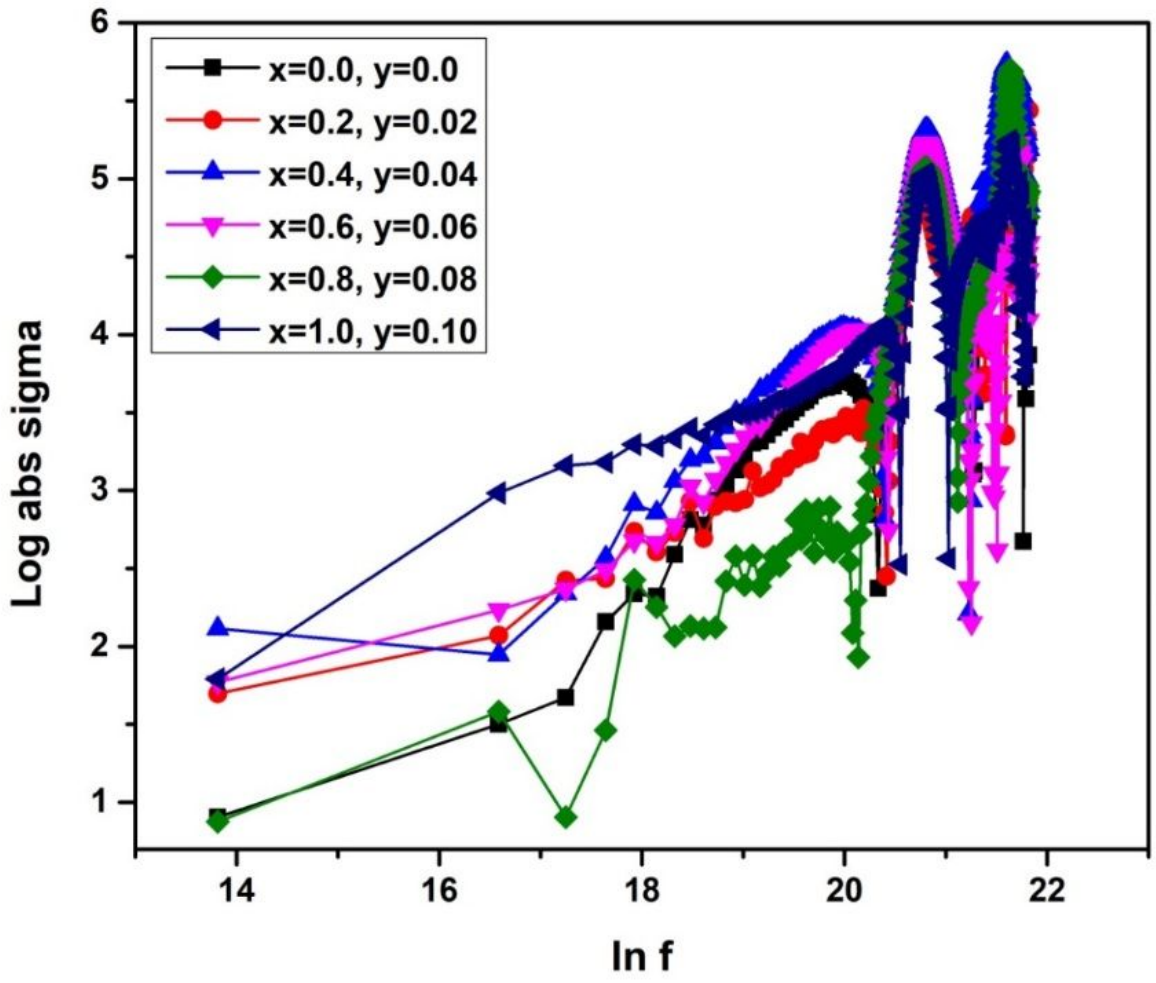

Figure 12

Log σ ac versus Log ω of CaBaCo2-xMnxYbyFe12-yO22where x=0.00 to 1.0 and y=0.00 to 0.1 hexagonal ferrites.

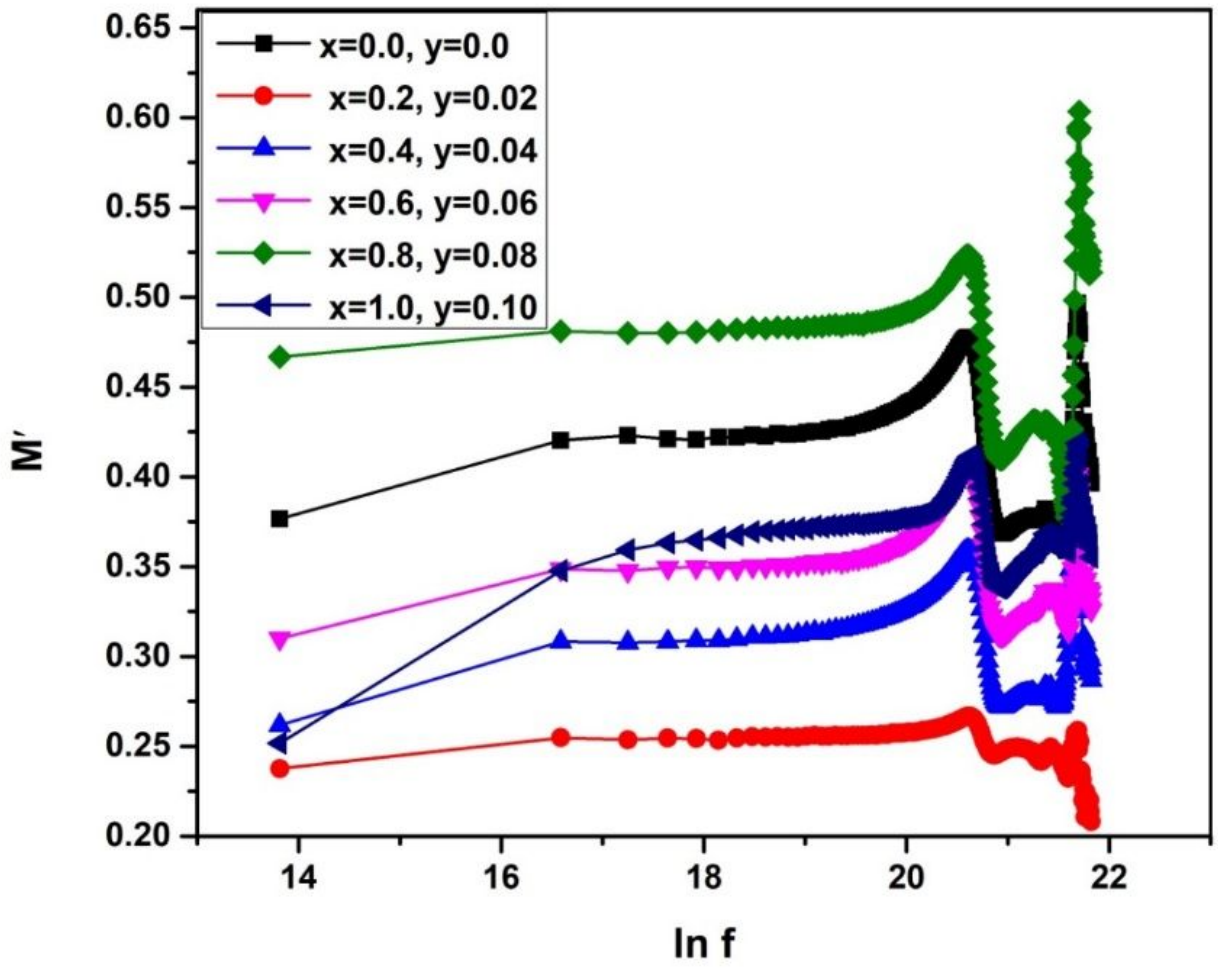

Figure 13

Frequency dependence real electric modulus (M') for CaBaCo2-xMnxYbyFe12-yO22where x=0.00 to 1.0 and y=0.00 to 0.1 hexagonal ferrites.

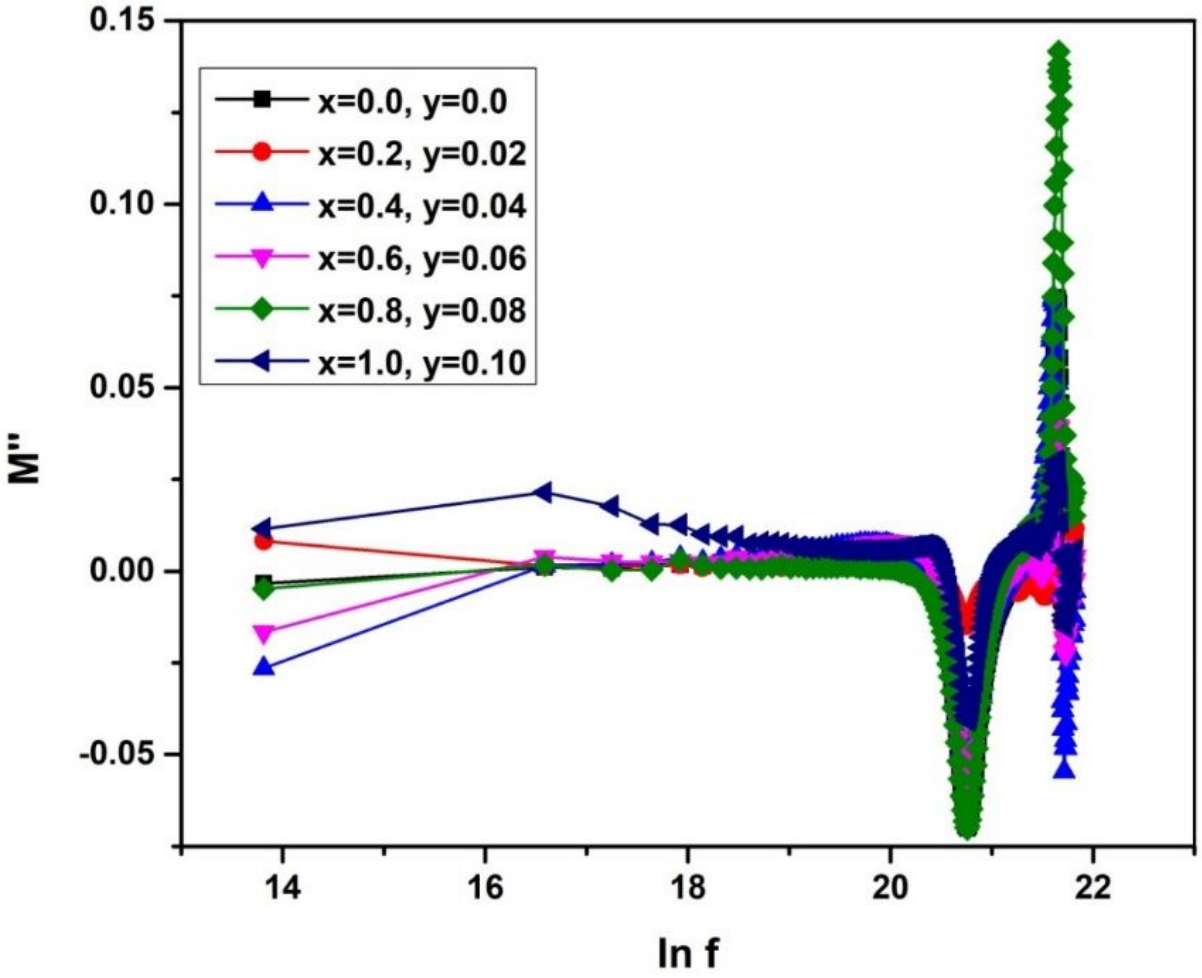

Figure 14

Frequency dependence imaginary electric modulus (M'') for CaBaCo2-xMnxYbyFe12-yO22where x=0.00 to 1.0 and y=0.00 to 0.1 hexagonal ferrites.

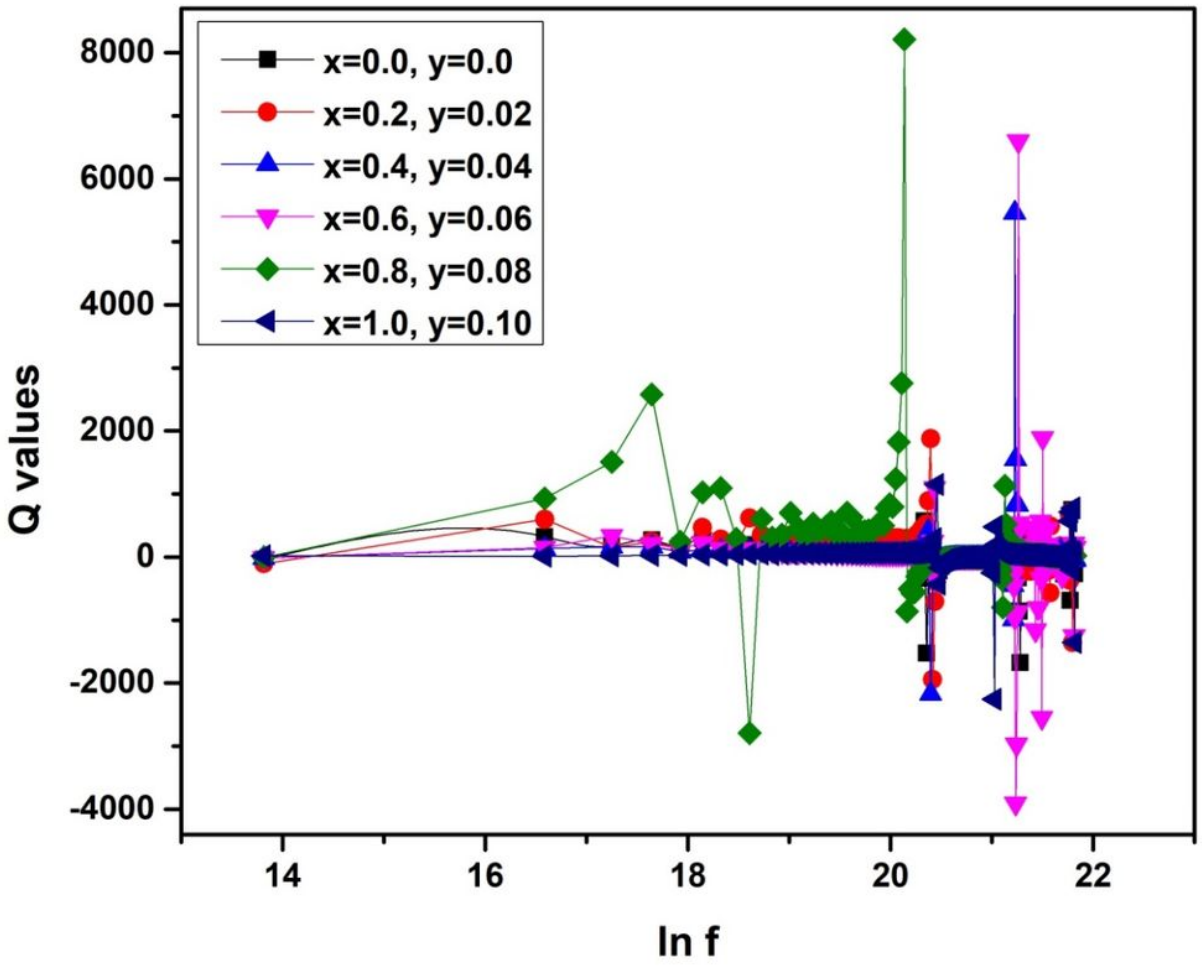

Figure 15

Frequency dependence imaginary electric modulus (M") for CaBaCo2-xMnxYbyFe12-yO22where x=0.00 to 1.0 and y=0.00 to 0.1 hexagonal ferrites..

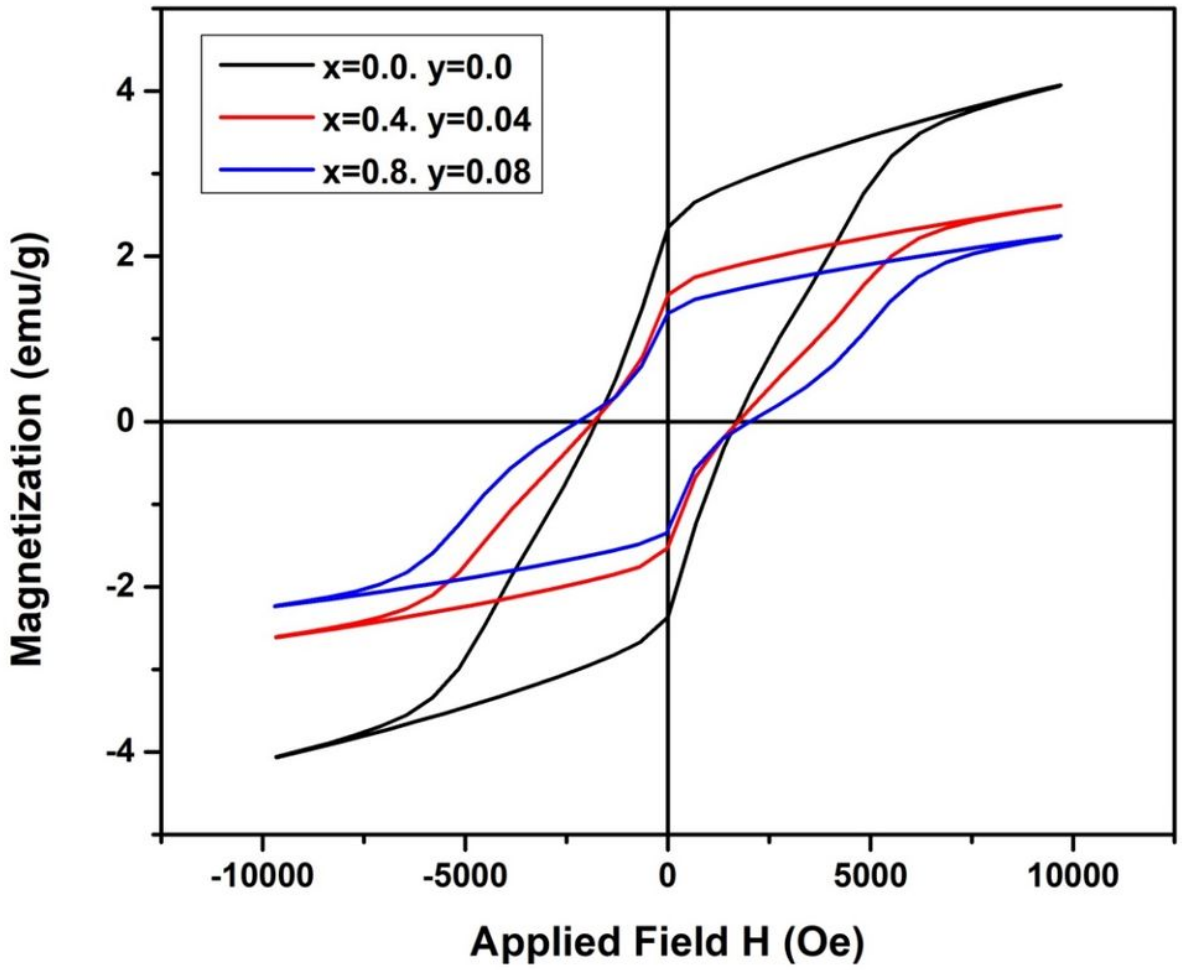

Figure 16

Frequency dependence imaginary electric modulus (M") for CaBaCo2-xMnxYbyFe12-yO22where x=0.00 to 1.0 and y=0.00 to 0.1 hexagonal ferrites.

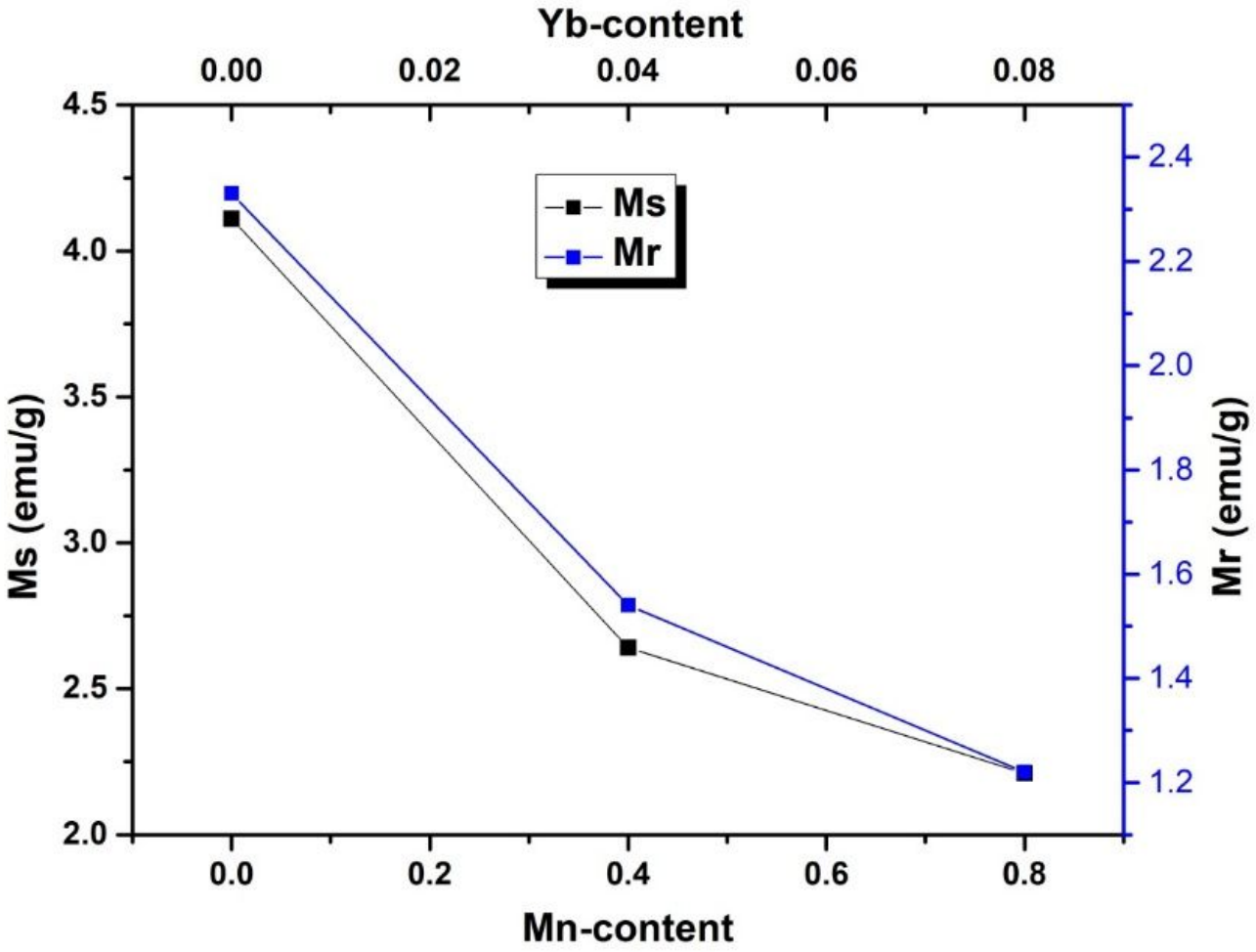

Figure 17

Variation in Ms and Mr against Mn-Yb content for CaBaCo2-xMnxYbyFe12-yO22where x=0.00 to 1.0 and y=0.00 to 0.1 hexagonal ferrites samples.

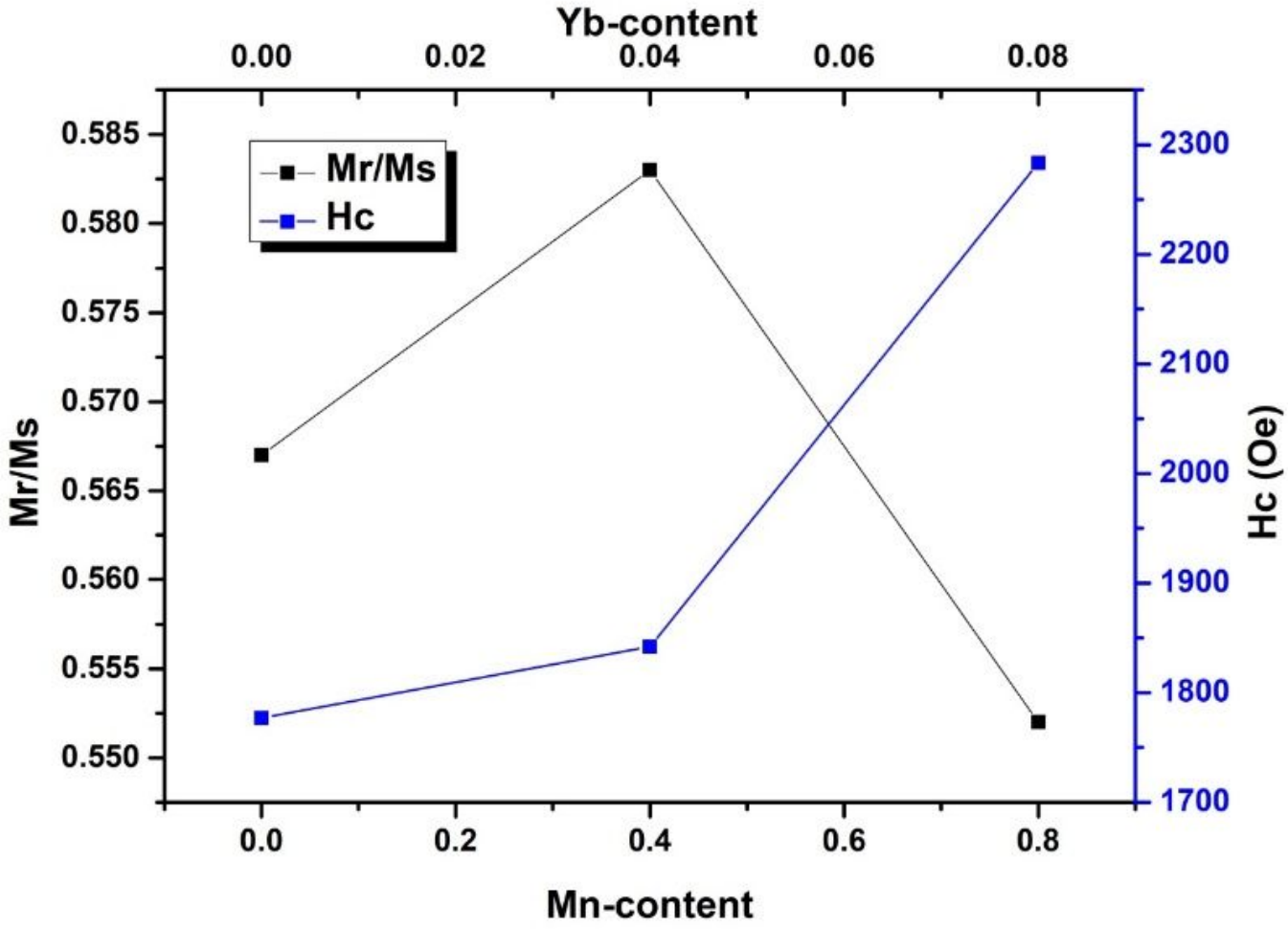

Figure 18

Mr/Ms vs Hc of CaBaCo2-xMnxYbyFe12-yO22where x=0.00 to 1.0 and y=0.00 to 0.1 hexagonal ferrites samples.

Supplementary Files

This is a list of supplementary files associated with this preprint. Click to download.

- Highlights.docx